Counting Fluorophores using Single-Photon Avalanche Diode Arrays for Single-Molecule Localization Microscopy

Heike Smedes

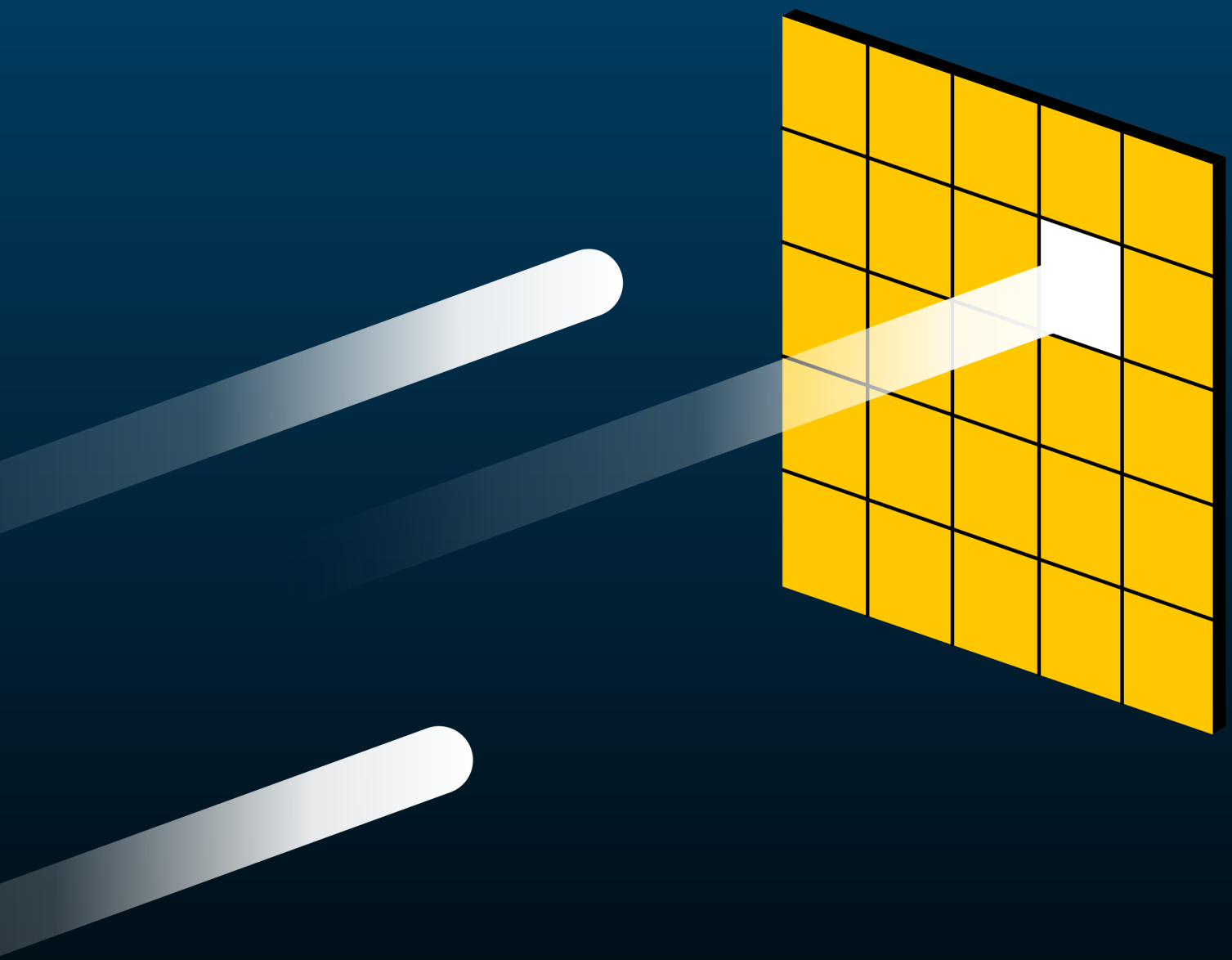

TU Delft

Counting Fluorophores using Single-Photon Avalanche Diode Arrays for Single-Molecule Localization Microscopy

by

Heike Smedes

to obtain the degree of Master of Science
at the Delft University of Technology,
to be defended on Monday June 17, 2024 at 1:00 PM.

Student number:	4750101	
Project duration:	October 2, 2023 – June 17, 2024	
Thesis committee:	Prof. dr. B. Rieger,	supervisor
	Prof. dr. S. Stallinga,	supervisor
	Dr. K. Grußmayer	
	Dr. I. Esmaeil Zadeh	

TU Delft

Acknowledgements

I would like to express my gratitude to all who supported me during my graduation project. In the past year, I have learned a lot and worked hard on my thesis of which the end result is laying in front of you, but this would not have been possible without the people around me.

First of all, I would like to thank my supervisors Bernd Rieger and Sjoerd Stallinga for trusting me with this project and guiding me throughout this year. At the beginning of the year, you gave me the choice between two projects: one with a clear goal and well-defined steps, and another that was slightly vague but potentially very exciting. I chose the latter, and together we figured out the steps on the way. In the weekly meetings on Thursday mornings, we had a lot of fun discussions, in which you could often give me a new perspective on the problem at hand.

In addition, I am grateful to Ludolf Meester for his input in the statistics part of my thesis. Intrigued by the mathematics and determined to solve it, our discussions and correspondence were of great value for my thesis.

I want to thank Jesse, Pim, Irene, Francisco, Achere, Simon, Bob, Luuk, Max, Menglin, and Gijs for the good vibes in the student rooms. This year would not have been the same without you. A special thanks goes out to Pim and Jesse, for choosing the colors of all my graphs and more.

Lastly, I would like to thank my friends, family, and especially Diego for listening to my thesis stories and for supporting me throughout the project.

Heike Smedes
Delft, May 2024

Abstract

For a long time, the resolution of light microscopy was restricted to approximately 200 nm, as described by Abbe's diffraction limit. Single-Molecule Localization Microscopy (SMLM) overcomes this limit by capturing many frames of a sample labeled with blinking fluorophores, where each frame shows a different subset of molecules. The fluorophores are located by fitting a model of their point spread function (PSF) and these localizations are combined to create an image with 20-50 nm resolution. Localizing a fluorophore is only possible when no other fluorescent molecules are active in the surrounding diffraction-limited area so that its PSF appears as an isolated blob. However, high-density regions unavoidably contain overlapping PSFs, which lead to localization errors as the number of emitters in the region of interest is unknown. To prevent this, the density of active fluorophores is typically kept between 0.01-0.1 μm^{-2} and data acquisition can take up to days, making dynamic imaging impossible. This theoretical research explores the possibility of enabling high-density SMLM by using Single-Photon Avalanche Diode (SPAD) arrays, detecting every incident photon with picosecond timing precision, instead of capturing the total intensity in a 10-100 ms interval like the conventionally used sCMOS cameras. The photon arrival times from simulated SPAD measurements are used to determine the number of emitters in the field of view, which is directly related to the second-order quantum coherence of the signal. This coherence can be calculated by dividing the arrival times into discrete time bins and convoluting the signal with itself. To correct the number of emitters for the bias that is introduced by the discretization of the data, an analytical expression is derived and validated with simulations. Using this correction, the number of Alexa647 fluorophores can be determined from a 0.1 ms simulated measurement with a relative standard error of 1% independent of emitter count, using a laser intensity of 330 kWcm^{-2} and 100% detection efficiency. Considering an experimental setting in which 10 kWcm^{-2} intensity and 10% detection efficiency are more realistic, a 1.5 s measurement is needed to obtain the same accuracy, and a 15 ms interval is required to obtain a standard error of 10%. The newly acquired information about the number of emitters will make it possible to locate fluorophores with overlapping point spread functions for multi-emitter fitting. Consequently, SPAD arrays will provide the ability to image high emitter densities, which enables faster data acquisition and dynamic imaging.

Contents

Acknowledgements v

Abstract vii

1 Introduction 1

2 Method 5
2.1 Forward Model . . . 5
2.2 Analysis of the Number of Emitters . . . 7

3 Results 9
3.1 Second-Order Quantum Coherence . . . 9
3.1.1 Coherent Light . . . 9
3.1.2 Antibunched Light . . . 10
3.1.3 Bin Size Dependency . . . 14
3.2 Estimation of the Number of Emitters . . . 17
3.2.1 Many Emitters . . . 19

4 Discussion 21
4.1 Main results . . . 21
4.2 Limitations . . . 22
4.3 Outlook . . . 23

5 Conclusion 25

References 27

A Interval Distribution for Non-Ideal Detection Efficiency 29

B Variance of the Second-Order Quantum Coherence 31
B.1 Derivation . . . 31
B.2 Moments of X . . . 34
B.3 Auxiliary Moments . . . 35
B.3.1 Moments of Y . . . 35
B.3.2 Moments of U . . . 35
B.3.3 Moments of Combinations of Y and U . . . 35
B.3.4 Moments of B . . . 36
B.3.5 Moments of Multiple B . . . 37

1. Introduction

Fluorescence light microscopy is one of the most important techniques available for biological research, enabling scientists to study tissues, cells, and small organisms. Samples are labeled with fluorescent markers, which attach only to specific locations, allowing researchers to visualize subcellular components and biological processes. A large advantage of this technique is that it works on living cells so that it is possible to track dynamic processes.

However, the resolution of optical microscopy is bounded by Abbe's diffraction limit ($\frac{\lambda}{2NA}$). Due to diffraction, every point source of light produces a blurred spot in the image plane, called point spread function (PSF). These spots are indistinguishable when multiple fluorophores are within a diffraction-limited area of each other, producing a blurry image. Consequently, the maximum achievable resolution for light microscopy is approximately 200 nm (fig. 1a). While this is sufficient to visualize subcellular components and bacteria, protein structures and interactions remain hidden[1].

Several methods have been developed in the last decades to overcome the diffraction limit, e.g. Single-Molecule Localization Microscopy (SMLM), which can achieve resolutions of 20-50 nm[2]. For this technique, samples are labeled with fluorescent dyes that stochastically switch *on* (emitting light) or *off* (not emitting light). Next, many frames are recorded using an sCMOS camera, which detects the total intensity coming from the sample during an exposure time of typically 10-100 ms[3]. As a result of the blinking behavior, all images show a different subset of fluorophores. In each frame, regions of interest (ROIs) are selected around the separate PSFs, and a PSF model is fit to each ROI to determine the fluorophore locations (fig. 1b). By combining all localizations, one super-resolution image is created (fig. 1c).

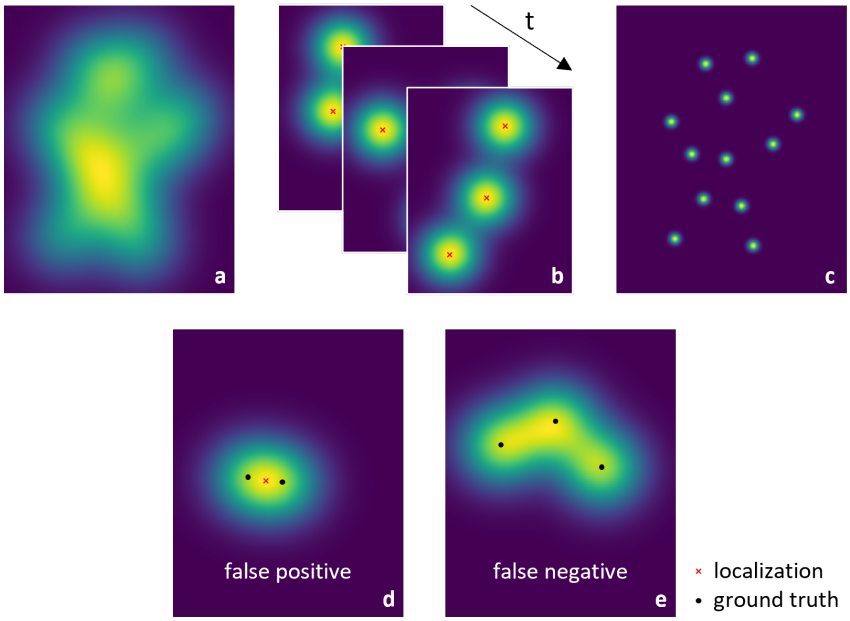

Figure 1: Simplified overview of Single-Molecule Localization Microscopy. (**a**) The resolution of conventional light microscopy is limited to 200 nm. (**b**) Many frames are captured, each showing a different subset of blinking fluorophores. The emitters are localized by fitting a PSF model to each blob. (**c**) A super-resolution image is generated by combining all localizations. (**d**) A false positive can occur when the superposition of multiple PSFs appears as the PSF of one emitter. (**e**) When the data does not resemble a single-molecule PSF, fitting results in a false negative.

A drawback of SMLM is that it only works for a low density of active emitters. This is because it is not feasible to fit a PSF model when multiple fluorophores within a diffraction-limited area are switched *on*. If the number of emitters within the ROI is unknown, the function space of the model is very large, leading to a high computational cost and the risk of getting stuck at a local minimum. Therefore, an ROI must contain the PSF of only one fluorophore.

However, some ROIs unavoidably cover multiple emitters, which causes localization errors[4]. This especially happens in high-density areas of samples, which are often of large interest. When a superposition of several PSFs appears as one bright spot on the detector, the algorithm might mistake it for a single-emitter PSF located in the center of the fluorophores, leading to a false positive localization (fig. 1d). Another problem can be that the single-emitter PSF cannot be fit to the ROI at all, which results in a false negative (fig. 1e). In that case, the data in the ROI is discarded. The final image might thus show emitters in places where they are not, and dark spots where many molecules should be visible, giving a false impression of the sample. To prevent these errors, the average density of active fluorophores is typically between 0.01-0.1 μm^{-2}[4, 5]. Consequently, data acquisition time ranges from minutes to several hours or even days, and dynamic imaging is impossible[1, 6].

Multiple methods have been proposed to process images with high emitter densities. Initial attempts, such as multi-emitter fitting[7] and a Bayesian approach named 3B[8] have shown to be too computationally expensive and unstable. Another approach is taken by SOFI[9], which exploits temporal and spatial correlations between the frames to improve the image quality. Although FALCON reaches a resolution of 100 nm for a density of 2.19 μm^{-2} using deconvolution, it is still worse than low-density methods [10–12]. A deep-learning technique, DECODE, has achieved a resolution of 50 nm for density of 0.85 μm^{-2}[5]. However, as neural networks rely strongly on training data, this is unsuitable for research into unknown structures.

As data processing methods have not delivered satisfactory results, altering the method of data acquisition may be more promising. Recently, a resolution of 60 nm was achieved for high-density SMLM using an event-based sensor, which captures only significant changes in light intensity rather than the intensity level[13]. Although this enables distinguishing emitters within a diffraction-limited area, the localization accuracy is limited as the intensity changes provide a limited amount of data points that can be used for localization.

Alternatively, a Single-Photon Avalanche Diode (SPAD) array can be used for acquiring data, which can detect individual photons with sub-nanosecond timing resolution. Although single-pixel SPADs have existed since the 1980s, multi-pixel arrays have only been successfully developed in the last two decades[14]. Each pixel consists of a p-n junction that is reverse-biased above its breakdown voltage. Consequently, the electric field in the depletion region is so high that a single incident photon can trigger a self-sustaining avalanche by creating an electron-hole pair. The rising edge of the resulting current marks the photon arrival time, which can be determined with a resolution of 10-100 ps[15]. Reported values of timing jitter are between 80-250 ps FWHM[14, 16, 17]. After a photon is detected, the SPAD array is reset to the initial conditions, a process that takes between 1-100 ns depending on the sensor. During this so-called dead time, no photons can be detected[15, 16, 18, 19].

The characteristics of SPAD arrays differ from sCMOS detectors in several ways. The quantum efficiency of SPAD sensors is currently between 10-50%, whereas sCMOS cameras detect $> 95\%$ of the incident photons[15, 20]. However, a large advantage of SPAD sensors is the absence of readout noise and thus, dark counts are their only source of noise. So-called primary dark counts occur at random due to thermally-generated carriers at rates between 0.3-100 cps μm^{-2}. In addition, the sensitivity of the sensors gives rise to secondary dark counts, which are correlated to the photon detections and can be distinguished into two categories[21]. Firstly, after-pulsing occurs when a charge carrier is captured in a deep-level trap of the detector during a detection avalanche, and is only released after the SPAD is already back in the initial condition, causing a new avalanche. This happens for 0.1-10% of the photon detections[15]. Secondly, dark counts are generated by cross-talk when an electroluminescence photon produced by one photon detection leads to another detection in a neighboring pixel. The fraction of photon detections that cause cross-talk depends on the excess voltage over the pixels and the distance separating the pixels[21]. As the SPAD technology advances quickly, it can be expected that the dead time, quantum efficiency and the dark count rates will further improve. In combination with the high timing precision and detection rate, this makes SPAD arrays a promising alternative for sCMOS cameras in SMLM.

Over the last decade, several studies have been performed on integrating single-photon sensors with SMLM. The first super-resolution images created with SPAD arrays were obtained in 2016[22]. The theoretical lower bound for localization accuracy of SPAD-based SMLM is comparable to the lower bound for sCMOS cameras[23]. Additionally, research was done into smart data compression

of SPAD measurements to compensate for the photon detection efficiency, improving the image resolution at the cost of losing timing information[24]. Furthermore, the correlation between the photon arrival times measured by a SPAD sensor was used to select frames with exactly one emitter in order to facilitate localization[25]. A disadvantage of this technique is that most available data is discarded.

This thesis further explores the possibilities of using a SPAD array for SMLM. As previously discussed, not knowing the number of emitters in an ROI is the main limitation of high-density imaging. When the fluorophore count is known, it can be used as an input to an adapted multi-emitter fitting algorithm, which reduces computational costs and improves accuracy. In this thesis, a method is developed to determine the number of emitters from simulated SPAD measurements. This is the first step in the development of an SMLM algorithm for SPAD arrays that can handle emitter densities up to 5 μm^{-2} and achieves 20-50 nm resolution, thus matching the high-density capabilities of DECODE and SOFI, while achieving the resolution that is currently obtained by low-density techniques.

The number of emitters in a sample can be determined by analyzing the statistical properties of the measured photon arrival times. As fluorophores are single-photon emitters, they can only emit one photon at a time and it takes some time to 'recharge' before the next photon can be emitted. The amount of simultaneously detected photons is thus an indicator of the number of fluorescent molecules in the ROI. The so-called second-order quantum coherence provides a measure to quantify this simultaneousness and to derive the exact number of molecules from the data.

In this research, an analytical expression is derived to extract the number of emitters from SPAD data. A computer model is made to simulate SMLM measurements on a SPAD sensor and the simulation outcomes are compared to the analytical results. The influence of laser power, fluorophore lifetime, and detection efficiency are investigated. In addition, the effect of the timing precision on the second-order quantum coherence, and thus on the emitter count, is assessed. In this research, dead time, dark counts, and background noise are neglected to simplify and understand the model and to obtain the best case results.

2. Method

This chapter describes how the number of emitters in a sample can be determined from simulated SPAD measurements for SMLM. In section 2.1, the simulation model is explained. Section 2.2 demonstrates how the fluorophore count can be derived from photon arrival times.

2.1 Forward Model

The forward model (fig. 2) simulates a measurement of a fluorescently labeled sample on a SPAD sensor. The sample is assumed to be illuminated for a time $\mathcal{T}$ by a laser with power P and wavelength λ_{ab}, which equals the absorption peak wavelength of the fluorescent molecules. During this interval, the fluorophores repeatedly absorb and release photons. The emitted photons have a wavelength $\lambda_{em} > \lambda_{ab}$ due to the Stokes shift. The light is focused onto the SPAD sensor by an objective with numerical aperture NA, and each photon is detected with a probability $\eta < 1$ by one of the sensor pixels. The resulting simulation consists of a sequence of photon arrival times per pixel.

After inserting emitter coordinates into the model (fig. 2a), the photon arrival times are generated. It is assumed that each fluorophore emits one fluorescence photon in every cycle of excitation and emission. Other processes, such as decay from the triplet state and non-radiative decay, are neglected. The intervals between photons can hence be modeled as the sum of the time it takes to absorb and to release a photon. Firstly, the excitation time T_{ex}, is distributed exponentially with a rate of $k_{ex} = \sigma_{ab} I$, which is the excitation rate of the fluorophore. Here, σ_{ab} denotes the absorption cross-section, and the photon flux I is determined by the laser power P and can be calculated using $I = \frac{P\lambda_{ab}}{\hbar c}$, in which $\hbar$ is the reduced Planck constant and c is the speed of light. Secondly, the emission time T_{em} depends on the lifetime τ_l, the average time for a fluorophore to emit a photon once it is excited. It can thus be modeled as an exponentially distributed variable with rate $k_{em} = \frac{1}{\tau_l}$. The total interval time T is the sum of these variables (fig. 2b),

$$T = T_{ex} + T_{em} \sim \mathrm{Exp}(k_{ex}) + \mathrm{Exp}\left(k_{em}\right), \tag{2.1}$$

and has an expected value of

$$\mathbb{E}[T] = \frac{1}{k_{ex}} + \frac{1}{k_{em}} = \frac{1}{\sigma_{ab} I} + \tau_l. \tag{2.2}$$

The arrival times of the photons are determined by calculating the cumulative sum of the photon intervals (fig. 2c).

Photons that arrive in an interval of length $\mathcal{T}$ are selected while those outside of the interval are discarded (fig. 2d). Selecting a random interval prevents correlation between the signals of different emitters as a result of the start-up phase of the simulation. Based on empirical data, discarding the data acquired during the first $10\mathbb{E}[T]$ is enough to achieve this. Subsequently, the detection efficiency $\eta < 1$ is applied, as there is a probability η that a photon is detected due to losses in the setup (lenses, mirrors, and filters), the objective (transmission rate, limited), and the sensor (quantum efficiency, fill factor). Therefore, photons are randomly discarded with a probability $1 - \eta$ (fig. 2e).

The remaining N photons are assigned spatial coordinates, for which a Gaussian PSF is assumed (fig. 2f). Although this model does not perfectly correspond to the actual shape of the PSF, it is a good approximation for freely rotating dipoles. Thus, the x- and a y-coordinates that are assigned to the detected photons are distributed as $\mathcal{N}(\mu_x, \sigma^2_{PSF})$ and $\mathcal{N}(\mu_y, \sigma^2_{PSF})$, respectively, where μ_x and μ_y are the input coordinates of the emitter. The standard deviation σ_{PSF} equals $0.25\lambda_{em}/\mathrm{NA}$, which is approximately equal to the value for which the Gaussian is the best fit for the PSF model[26, 27].

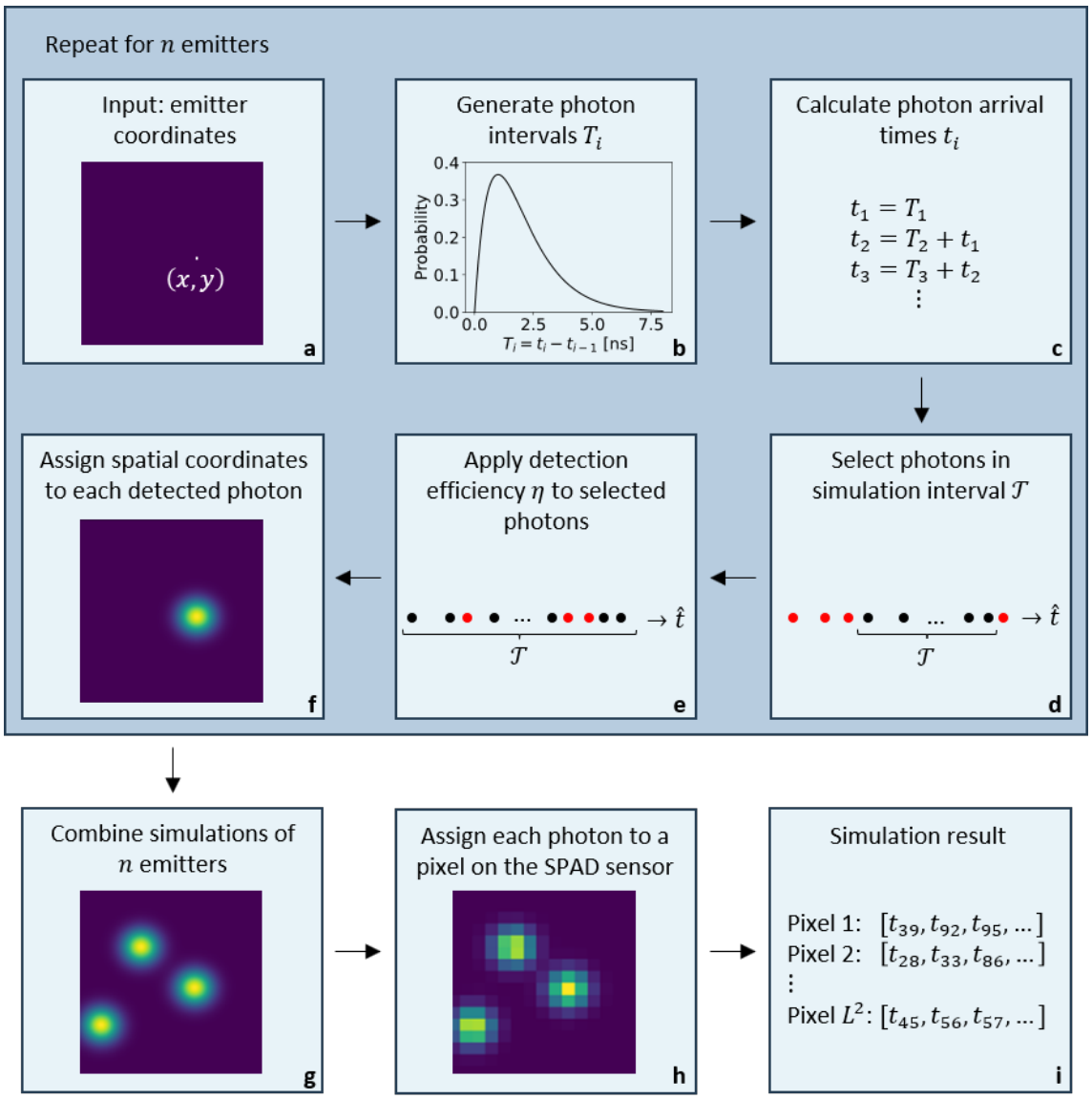

Figure 2: Steps for simulating an SMLM measurement on a SPAD array. (**a**) The position of the emitter is randomly generated. (**b**) Time intervals between are generated from a hypoexponential distribution. (**c**) The photon arrival times are a cumulative sum of the interval times. (**d**) Photons in an interval $\mathcal{T}$ are selected, and the others are discarded. (**e**) Every photon has a probability of η of being detected. (**f**) Spatial coordinates are assigned to the remaining photons, which together construct the PSF. Steps (**a** - **f**) are repeated for every emitter. (**g**) All PSFs are combined. (**h**) The measurement is discretized. (**i**) The final measurement consists of a list of photon arrival times per pixel.

Steps a-f of fig. 2 are repeated for n emitters. The PSFs of all emitters are then combined and a 2D histogram of L^2 bins is created (fig. 2g,h). Each bin represents one pixel on the SPAD sensor. The ideal pixel size could be determined by optimizing the SMLM model. However, since this model has not yet been developed for SPAD sensors, a pixel size of $\Delta l = 0.25\lambda_{em}/\text{NA}$ is assumed, which satisfies the Nyquist sampling criterion. This way, a large field of view is recorded while no information is lost. In the final step of the forward model, a list of photon arrival times is created for every pixel (fig. 2i).

In this research, the emitters that are simulated are Alexa647 molecules. This fluorescent dye is widely used for super-resolution microscopy. Its absorption and emission peak wavelengths are $\lambda_{ab} = 650$ nm and $\lambda_{em} = 665$ nm, respectively. The absorption cross-section is approximately $9.1 \cdot 10^{-16}$ cm^2 and the fluorescent lifetime is 1 ns[28, 29]. Whereas commonly used frame times for SMLM are in the order of 100 ms, here, an illumination time of $\mathcal{T}_0 = 0.1$ ms is chosen[2]. This is much larger than the lifetime of the singlet state, but small compared to the triplet lifetime ($\sim$ ms) such that it can be assumed that none of the detected photons originate from triplet state decay[30]. The simulation constants are summarized in table 2.1.

Table 2.1: The simulation constants with their symbols and the values used in this research.

Constant	Symbol	Value
Absorption peak wavelength	λ_{ab}	650 nm
Emission peak wavelength	λ_{em}	665 nm
Absorption cross section	σ_{ab}	$9.1 \cdot 10^{-16}$ cm^2
Fluorescent lifetime	τ_l	1 ns
Numerical aperture	NA	1
Standard deviation of PSF	σ_{PSF}	$0.25\lambda_{em}/\text{NA} = 166.25$ nm
Pixel size	Δl	$0.25\lambda_{em}/\text{NA} = 166.25$ nm
Number of pixels	L^2	32^2
Illumination time	$\mathcal{T}$	$\mathcal{T}_0 = 0.1$ ms
Detection efficiency	η	$0 \leq \eta \leq 1$

2.2 Analysis of the Number of Emitters

An important property of fluorophores is that they are single-photon emitters, meaning that they only emit one photon at a time. Consequently, if two photons are detected simultaneously, at least two emitters must be in the field of view. This principle is used to determine the number of emitters in the sample.

The photon arrival times are analyzed with the second-order quantum coherence. This function calculates the autocorrelation of the measured intensity $I(t)$ and is defined as

$$g^{(2)}(\tau) = \frac{\langle I(t)I(t+\tau)\rangle}{\langle I(t)\rangle \langle I(t+\tau)\rangle} = \frac{\langle I(t)I(t+\tau)\rangle}{\langle I\rangle^2}. \tag{2.3}$$

The second equality holds provided that the average intensity is constant, which can be assumed when the laser power is constant and the fluorophores do not blink during the measured interval. Neglecting background noise, the total intensity of n fluorophores equals

$$I(t) = \sum_{j=1}^{n} i_j(t), \tag{2.4}$$

where $i_j(t)$ denotes the intensity of emitter j at time t. Assuming that each emitter has an average intensity $\langle i\rangle$, the mean intensity is given by

$$\langle I\rangle = n \langle i\rangle . \tag{2.5}$$

By substituting eq. (2.4) and eq. (2.5) in eq. (2.3), and separating the terms where $j \neq k$ and $j = k$, the coherence can be written as

$$\begin{aligned} g^{(2)}(\tau) &= \frac{\left\langle \sum_{j=1}^{n} i_j(t) \sum_{k=1}^{n} i_k(t+\tau) \right\rangle}{n^2 \langle i\rangle^2} \\ &= \frac{n(n-1)\langle i\rangle^2 + n\langle i(t)i(t+\tau)\rangle}{n^2\langle i\rangle^2} \\ &= 1 - \frac{1}{n} + \frac{1}{n}\frac{\langle i(t)i(t+\tau)\rangle}{\langle i\rangle^2}. \end{aligned} \tag{2.6}$$

The intensity per molecule i is proportional to the detection efficiency η and the probability $p(t)$ of emitting a photon at time t. Therefore, eq. (2.6) can be written as

$$g^{(2)}(\tau) = 1 - \frac{1}{n} + \frac{1}{n}\frac{\eta^2\langle p(t)p(t+\tau)\rangle}{\eta^2\langle p\rangle^2} = 1 - \frac{1}{n} + \frac{1}{n}\frac{\langle p(t)p(t+\tau)\rangle}{\langle p\rangle^2}, \tag{2.7}$$

where $g^{(2)}(\tau)$ is a function of the conditional probability of a fluorophore emitting a second photon at time $t+\tau$, given that a photon was emitted at t. As can be seen, the detection efficiency η cancels out of the equation and it does not affect the second-order quantum coherence[31–33].

For coherent light, the second-order coherence is constant over time (fig. 3a). The photons in a beam of this type of light are Poisson distributed in space and the intervals separating them

are exponentially distributed. For this reason, $p(t)$ is independent of $p(t+\tau)$ and $\langle p(t)p(t+\tau)\rangle = \langle p(t)\rangle \langle p(t+\tau)\rangle$. Equation 2.7 then simplifies to

$$g^{(2)}(\tau) = 1. \tag{2.8}$$

Fluorophores emit a type of light that is more constant than coherent light, because the intervals between the photons are more regular. The coherence of this light can be derived by writing the conditional probability of eq. (2.7) in terms of the probability p_s of a fluorophore being excited in the singlet state[33]. The probability of detecting a photon in any moment ($\langle p \rangle$) is proportional to the steady-state probability $p_s(\infty)$ that a molecule is excited. Additionally, the probability of detecting a second photon at time $t+\tau$ is proportional to the evolution of $p_s(\tau)$, with the initial condition that $p_s(\tau) = 0$ since it is certain that the fluorophore is in the ground state, as a photon was just emitted. Therefore, the conditional probability can be written as

$$\frac{\langle p(t)p(t+\tau)\rangle}{\langle p\rangle^2} = \frac{p_s(\tau)}{p_s(\infty)}. \tag{2.9}$$

Following the derivation in [32] and [33], the probability $p_s(t)$ can be found through the rate equations:

$$\frac{d}{dt}\begin{pmatrix} p_g \\ p_s \end{pmatrix} = \begin{pmatrix} -k_{ex} & k_{em} \\ k_{ex} & -k_{em} \end{pmatrix}\begin{pmatrix} p_g \\ p_s \end{pmatrix}. \tag{2.10}$$

For short timescales, only the occupation levels of the ground state, p_g, and the singlet state, p_s, have to be considered. The solution to eq. (2.10) is given by

$$\begin{pmatrix} p_g \\ p_s \end{pmatrix} = \begin{pmatrix} 1 & 1 \\ -1 & -\frac{k_{ex}}{k_{em}} \end{pmatrix}\begin{pmatrix} c_1 e^{-(k_{ex}+k_{em})t} \\ c_2 \end{pmatrix}, \tag{2.11}$$

where c_1 and c_2 are constants depending on the initial conditions. Here, $p_g(0) = 1$ and $p_s(0) = 0$, giving

$$\frac{p_s(t)}{p_s(\infty)} = 1 - e^{-(k_{ex}+k_{em})\tau} \tag{2.12}$$

so that eq. (2.7) reduces to

$$g^{(2)}(\tau) = 1 - \frac{1}{n}e^{-k\tau}, \quad k = k_{ex} + k_{em}. \tag{2.13}$$

An example of antibunching is shown in fig. 3b. The conditional probability of emitting a photon immediately after the previous is almost zero. Therefore, the coherence has its minimum at $\tau = 0$ and increases with τ. When τ is large compared to $\mathbb{E}[T]$, the signals at t and $t+\tau$ are uncorrelated and the coherence converges to 1. Light that satisfies the property $g^{(2)}(0) < g^{(2)}(\tau)$ is said to be *antibunched*. At $\tau = 0$, eq. (2.13) simplifies to

$$g^{(2)}(0) = 1 - \frac{1}{n}, \tag{2.14}$$

which directly relates the coherence to the number of emitters in the sample.

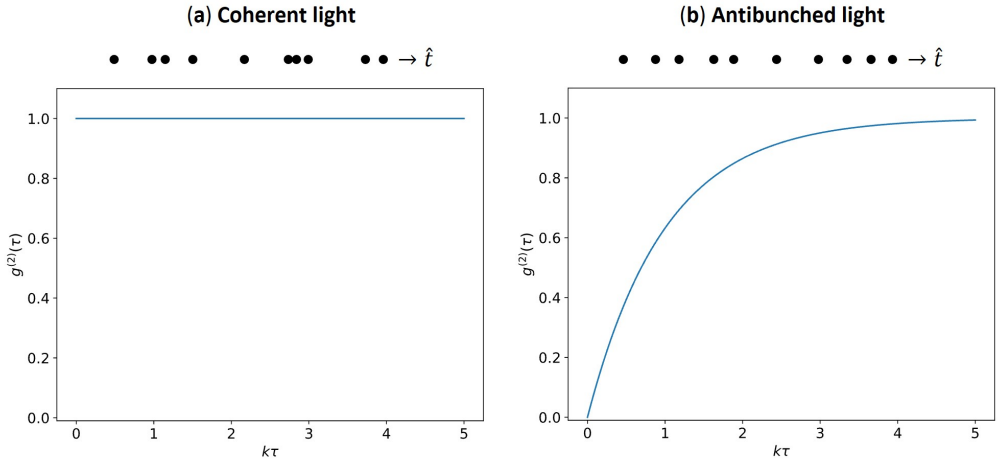

Figure 3: The second-order quantum coherence function $g^{(2)}(\tau)$. (**a**) For Poisson distributed photons result $g^{(2)}(\tau) = 1$. (**b**) For approximately uniformly distributed photons $g^{(2)}(\tau) = 1 - \frac{1}{n}e^{-k\tau}$, where $n = 1$ in this case.

3. Results

In section 3.1, the discrete-time second-order quantum coherence is derived. This equation is then compared to simulations of coherent and antibunched light. Next, the influence of various parameters on the coherence is discussed, which include the excitation and emission rate, detection efficiency and bin size.

Section 3.2 focuses on determining the number of emitters from a measurement. The knowledge obtained about the coherence is used to provide a reliable estimate of the amount of molecules in a sample.

3.1 Second-Order Quantum Coherence

The second-order coherence is determined from the recorded data by analyzing the photon arrival times of the whole sensor. Because the intensity I is proportional to the photon count $c(t)$ at the detector, eq. (2.3) can be written as

$$g^{(2)}(\tau) = \frac{\langle c(t)c(t+\tau)\rangle}{\langle c\rangle^2}, \tag{3.1}$$

where $\langle c\rangle^2$ equals the square of the detection rate and the denominator denotes the average number of photon pairs separated by lag τ.

Equation (3.1) is discretized by dividing the measurement interval $\mathcal{T}$ into m bins of size Δt. Let C_i be the number of photons observed in bin i, where $i\Delta t \leq t < (i+1)\Delta t$. Then, the number of photon pairs with a lag of ℓ bins is calculated by summing $C_iC_{i+\ell}$ over all bins. At $\ell = 0$, the number of pairs is corrected by subtracting N, since every photon forms a pair with itself. Consequently, the discrete-time second-order coherence is formulated as

$$g^{(2)}[\ell] = \frac{\frac{1}{m-\ell}\left(\sum_{i=1}^{m-\ell} C_iC_{i+\ell} - N\delta[\ell]\right)}{(N/m)^2} = \frac{m^2}{N^2(m-\ell)}\left(\sum_{i=1}^{m-\ell} C_iC_{i+\ell} - N\delta[\ell]\right). \tag{3.2}$$

3.1.1 Coherent Light

To simulate coherent light, exponentially distributed photon intervals have to be generated. Therefore, the Alexa647 fluorophores are assumed to re-excite instantaneously after emitting a photon. The interval time then only depends on the lifetime and is distributed as

$$T \sim \mathrm{Exp}\left(\frac{1}{\tau_l}\right). \tag{3.3}$$

The resulting second-order coherence is shown in fig. 4. As can be seen, $g^{(2)}[\ell] \approx 1$ for all ℓ, which is in agreement with the theory.

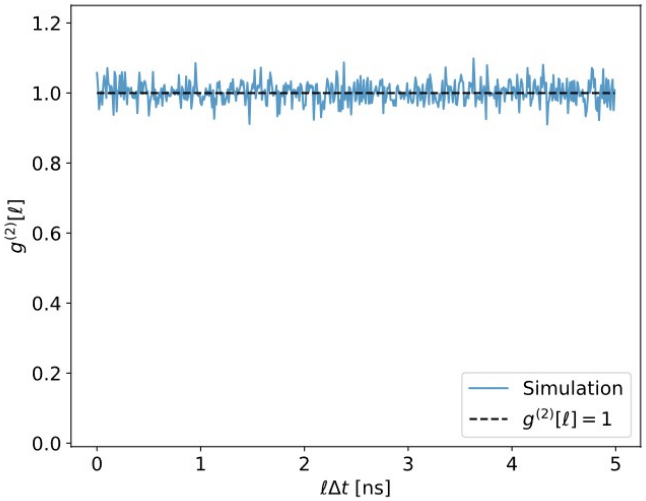

Figure 4: The second-order quantum coherence for coherent light of one emitter, where $\mathbb{E}[T] = 1$ ns, $\mathcal{T} = 0.1$ ms, and $\Delta t = 0.01$ ns. For coherent light $g^{(2)}[\ell] = 1$.

3.1.2 Antibunched Light

Antibunched light occurs when the photons are distributed more regularly than a Poisson distribution. This happens when the excitation time of the molecules is accounted for and the interval distribution is a sum of exponential distributions (eq. (2.1)). In that case, the second-order quantum coherence $g^{(2)}(\tau)$ satisfies the condition for antibunching ($g^{(2)}(0) < g^{(2)}(\tau)$). The following sections discuss the influence of the rate parameters, k_{ex} and k_{em}, and the detection efficiency η on the coherence.

Equal rates

When the rate parameters are equal ($k_{ex} = k_{em}$), the antibunching effect is the strongest. Figure 5 shows the coherence of light emitted by 1 to 4 fluorophores. In these simulations, the laser power was chosen to be 330 kWcm^{-2} so that the excitation rate was equal to the emission rate of 1 ns^{-1}. The results closely match the theory (eq. (2.13)), which is indicated by the dashed line.

The second-order coherence can be derived analytically for $k_{ex} = k_{em} \equiv \lambda$. In this case, the photon interval distribution simplifies to

$$T \sim \text{Exp}(\lambda) + \text{Exp}(\lambda) \sim \text{Gam}(2, \lambda). \tag{3.4}$$

The conditional probability of detecting a second photon of a fluorophore at $t + \tau$, given that one was found at t is

$$\frac{\langle p(t)p(t+\tau)\rangle}{\langle p\rangle^2} = \frac{\langle p\rangle \langle p(t+\tau|t)\rangle}{\langle p\rangle^2} = \frac{2}{\lambda}\sum_{i=1}^{\infty} Gam(\tau; 2i, \lambda) = 1 - e^{-2\lambda\tau} = 1 - e^{-k\tau}, \tag{3.5}$$

where the probability of measuring a photon, $\langle p\rangle$, equals the total rate $\lambda/2$. The conditional probability of detecting a second photon, $\langle p(t+\tau|t)\rangle$, is calculated by summing the probabilities of finding the i^{th} next photon at τ. Because the interval between the current and the i^{th} next photon is a sum of $2i$ Exp(λ) random variables, these probabilities are given by the probability density function of the Gam($2i, \lambda$) distribution. Substituting the result of eq. (3.5) into eq. (2.7), yields the expected result of

$$g^{(2)}(\tau) = 1 - \frac{1}{n}e^{-k\tau}. \tag{3.6}$$

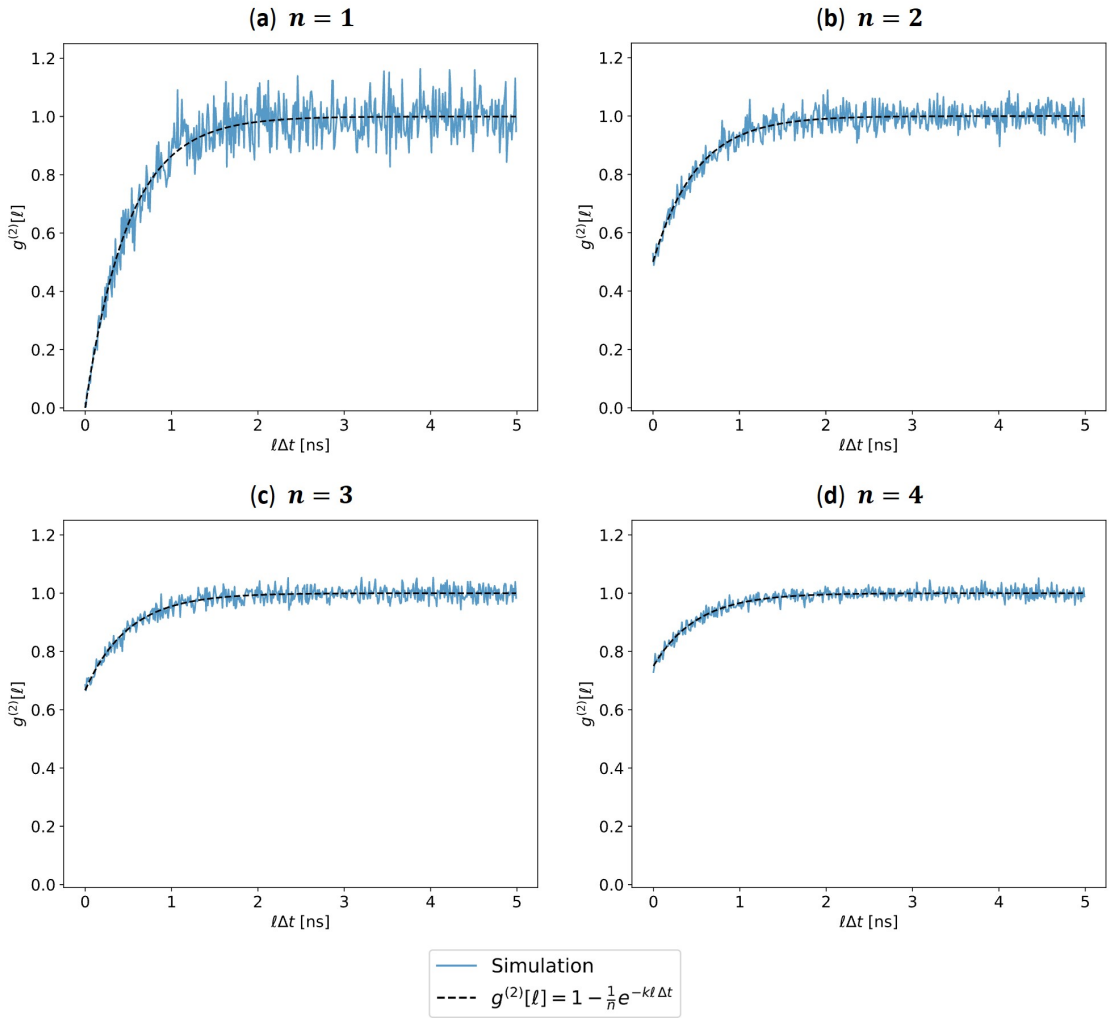

Figure 5: The second-order quantum coherence for different numbers of fluorophores, where $k = 2$ ns^{-1}, $\mathbb{E}[T] = 2$ ns and $\Delta t = 0.01$ ns.

Unequal Rates

It is not a given that the rate parameters are always equal. A laser power of 330 kWcm^{-2} is very high and causes photobleaching quickly. Therefore, in an experimental set-up, a lower intensity is preferred and it is likely that $k_{ex} \neq k_{em}$. In that case, antibunching also occurs, although the effect is less strong.

In the first example, the expected interval time $\mathbb{E}[T]$ was the same as before (2 ns), while the rate parameters were different. The laser power was 168 kWcm^{-2} so that $\mathbb{E}[T_{ex}] = 1.98$ ns and the fluorophore lifetime was set at 0.0198 ns. Therefore, $k_{ex} = 0.5$ and $k_{em} = 50.5$ ns^{-1}, giving $k = 51$ ns^{-1}.

The simulation results are shown in fig. 6a. Because k is much higher, the coherence converges to 1 much faster than in fig. 5a. In the limit of $k \to \infty$, the coherence converges to 1, in which case the light is coherent. This happens when either the excitation time or the emission time is negligible and the distribution of the interval times is exponential. Here, the characteristic antibunching shape appears again by using a smaller bin size and looking at the first part of the signal(fig. 6b). It should be noted that, for experimental data, the bin size is limited by the timing uncertainty, as Δt should be larger than the timing resolution of the experiment.

Next, k is kept constant instead of $\mathbb{E}[T]$. In this simulation, the laser power was 6.6 kWcm^{-2}, such that $k_{ex} = 0.0198$ ns^{-1}, which is more realistic in an experimental setting. The lifetime of the molecule was $\tau_l = 0.505$ ns, giving $k_{em} = 1.98$ ns^{-1}, and so $k = 2$ ns^{-1}. With these parameters, the average interval time increased to $\mathbb{E}[T] = 51$ ns, which is approximately a factor 25 higher than before. Consequently, 25 times less photons were detected in the standard measuring interval of $\mathcal{T}_0 = 0.1$ ms. Therefore, it was increased to $\mathcal{T} = 25\mathcal{T}_0 = 2.5$ ms.

Figure 7a shows the simulation result together with the theoretical curve. As $k = 2$ ns^{-1}, the graph looks the same as in fig. 5a. However, there is a clear increase in the variation of the

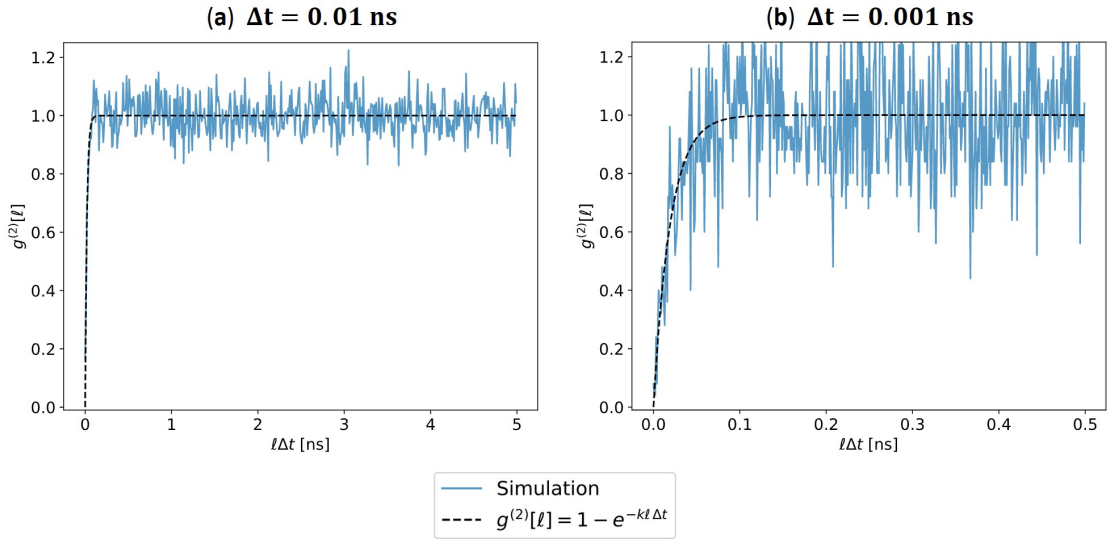

Figure 6: The second-order quantum coherence for $n = 1$, where $k = 51$ ns^{-1} and $\mathbb{E}[T] = 2$ ns. (**a**) The high value of k causes a steep incline in the coherence. (**b**) By decreasing the bin size, the characteristic curve for antibunching becomes visible again.

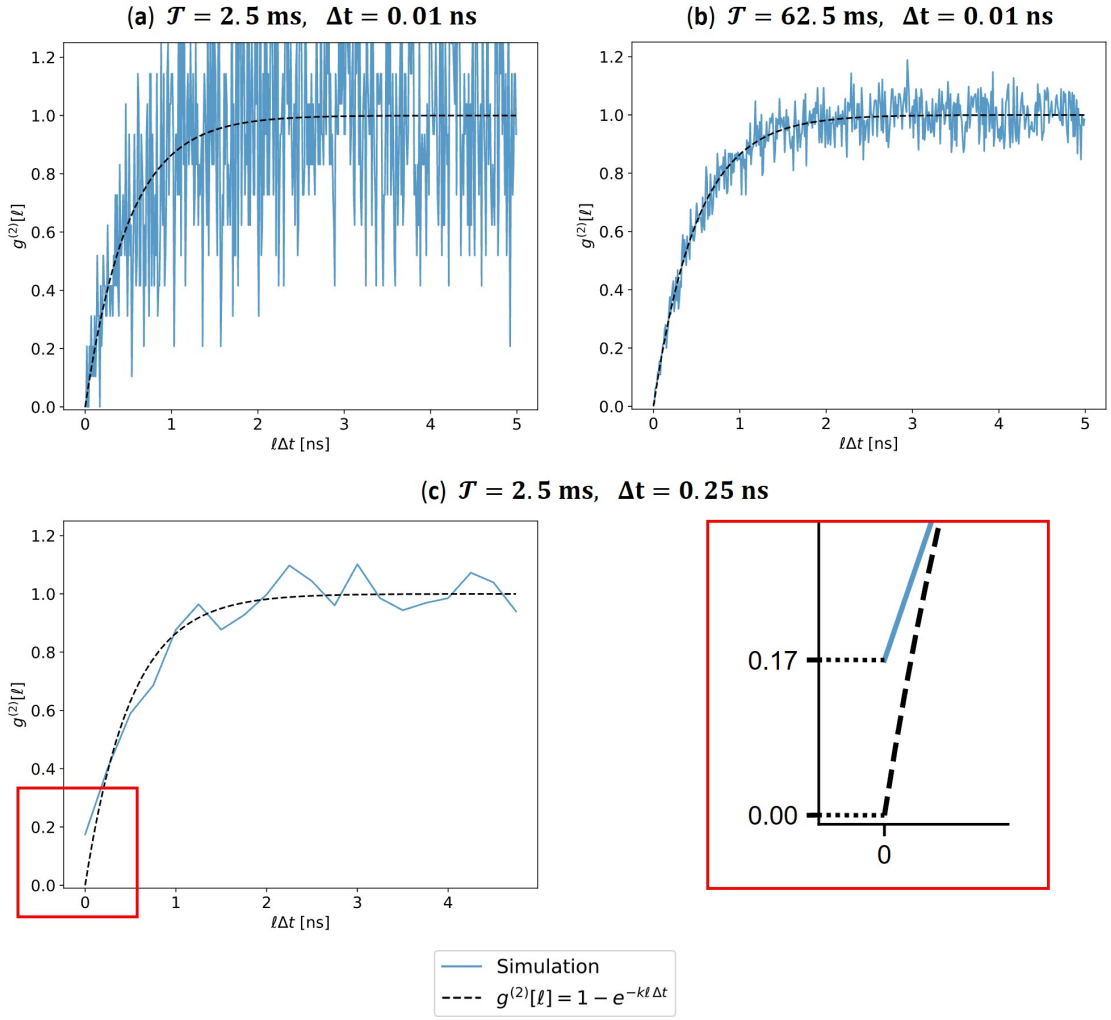

Figure 7: The second-order quantum coherence for $n = 1$, where $k = 2$ ns^{-1} and $\mathbb{E}[T] = 51$ ns. (**a**) The long photon intervals cause a larger variance, which can be reduced by (**b**) increasing the measurement interval, or (**c**) increasing the bin size. However, larger bin sizes cause a bias (see red box).

curve. The reason for this is that the same number of photons is distributed over a longer interval. Therefore, the signal is sparser, and the variance is higher. By extending the measurement interval to $25^2\mathcal{T}_0 = 62.5$ ms, this effect is counterbalanced, resulting in similar noise levels (fig. 7b). Thus, when k is constant and $\mathbb{E}[T]$ is increased by a factor a, the measurement time $\mathcal{T}$ has to be multiplied by a^2 to maintain the same accuracy for estimating the curve.

Increasing the measurement interval might not always be feasible, as triplet decay or photobleaching may affect the measurements. Then, another solution to reduce the variance is to increase the bin size. In fig. 7c the bin size Δt is increased from 0.01 to 0.25 ns, while the measurement interval is $25\mathcal{T}_0 = 2.5$ ms. Although this reduces the variance significantly, it also introduces a positive bias for small $\ell\Delta t$. As can be seen from the red box, the coherence equals $g^{(2)}[0] = 0.17$ instead of 0. This is because the bin contains information about the entire first bin, instead of a point in time. Whereas the probability of measuring multiple photons within the same bin is almost zero when the bin size is small, it increases when the bins are extended. Therefore, the coherence increases.

Detection Efficiency

So far, the detection efficiency η was assumed to be 1, meaning that all emitted photons lead to a detection event. However, experimental SMLM set-ups generally only reach efficiencies between 1-20%. Therefore, it is useful to analyze how η affects the coherence.

When the detection efficiency is smaller than 1, the distribution of photon detection intervals changes (appendix A). The average time between the detections increases to $\mathbb{E}[T'] = \mathbb{E}[T]/\eta$, while the excitation and emission rates of the fluorophores stay the same. Consequently, the sum of

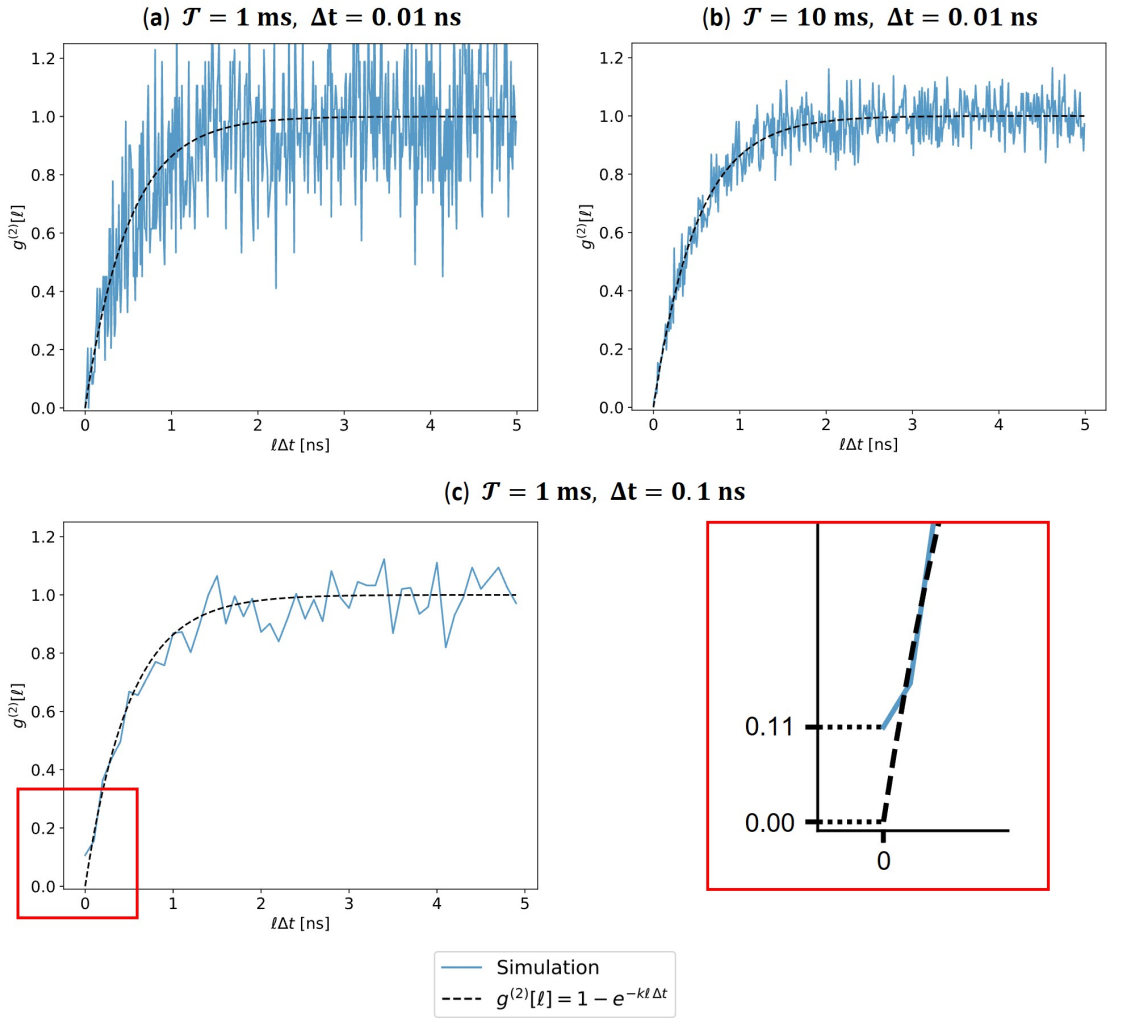

Figure 8: The second-order quantum coherence for $n = 1$, where $\eta = 0.1$, the expected interval time is $\mathbb{E}[T'] = \eta^{-1}\mathbb{E}[T] = 20$ ns and $k' = k = 2$ ns^{-1}. (**a**) The low detection efficiency causes a larger variance, which can be reduced by (**b**) increasing the measurement interval, or (**c**) increasing the bin size. However, larger bin sizes cause a bias (see red box).

rates remains $k' = k$. Since $g^{(2)}[\ell]$ is fully determined k and n, the coherence is thus unaffected by the detection efficiency. This observation is in agreement with the theoretical framework, where η cancels out of the equation (eq. (2.7)). This may seem counterintuitive, as the detection efficiency is usually a limiting factor in physics research. However, in this case, it is the distance between subsequently emitted photons that counts, and that is unaffected by the detection efficiency. Thus, the only consequence of a low detection efficiency, is that it takes more time to acquire the same amount of photons.

For the following simulation, a detection efficiency of 10% was assumed ($\eta = 0.1$). The excitation and emission rate were $k_{ex} = k_{em} = 1$ ns^{-1} so that $k = 2$ ns^{-1} and $\mathbb{E}[T'] = 20$ ns. A measurement time of $\mathcal{T} = \eta^{-1}\mathcal{T}_0 = 1$ ms was used to ensure that the number of detected photons was comparable to earlier examples.

The result is shown in fig. 8a. Like in the previous example, the graph follows the expected curve, but its variance is high. Following the same reasoning as before, improving the accuracy is possible by extending the measurement interval to $\mathcal{T} = \eta^{-2}\mathcal{T}_0 = 10$ ms (fig. 8b).

Reducing variance is also possible by increasing the bin size (fig. 8c). Again, this method introduces a bias as each bin provides information about a Δt interval. Here, a coherence of 0.11 was measured, whereas 0 was expected. It is important to note that different detection efficiencies give an equal bias, provided that $\eta_1^2\mathcal{T}_1 = \eta_2^2\mathcal{T}_2$ so that their variance is comparable. The reason for this is that, if two subsequently emitted photons are both detected, the interval between them is $\mathrm{Exp}(k_{ex}) + \mathrm{Exp}(k_{em})$ distributed, regardless of η. Thus, increasing the bin size does not lead to a different amount of photons and photon pairs per bin for different detection efficiencies.

3.1.3 Bin Size Dependency

The value of the coherence at $\tau = 0$ is needed to determine the number of emitters in the sample. Using eq. (2.14), the number of molecules n is given by

$$n = \left(1 - g^{(2)}(0)\right)^{-1}. \tag{3.7}$$

However, $g^{(2)}[0]$ deviates slightly from $g^{(2)}(0)$, as it is discrete and thus provides information about the entire first bin instead of a point in time. This deviation is the bias that was observed in fig. 7c and fig. 8c, where the coherence for small $\ell\Delta t$ is larger than expected. If the bin size is small enough compared to k, the bias does not affect the fluorophore count. However, the bin size is restricted by the timing precision of the SPAD array. With a timing resolution of 100 ps and 250 ps FWHM jitter, a bin size of at least 0.35 ns should be used, preferably larger. As fig. 7c and fig. 8c show, bin sizes of 0.25 ns and 0.1 ns, respectively, already caused a substantial bias. Therefore, it is necessary to gain a deeper understanding of the dependency of the coherence on the bin size.

The expected value of the coherence at $\ell = 0$ is given by eq. (3.2). Using the linearity of the expectation operator

$$\mathbb{E}\left[g^{(2)}[0]\right] = \frac{m}{\mathbb{E}[N]^2}\left(\sum_{i=1}^{m}\mathbb{E}\left[C_i^2\right] - \mathbb{E}[N]\right) = \frac{m^2}{\mathbb{E}[N]^2}\mathbb{E}\left[C_i^2\right] - \frac{m}{\mathbb{E}[N]}, \tag{3.8}$$

where $\mathbb{E}\left[C_i^2\right]$ is the expected value of the square of the photon count per bin. With the help of Dr. L. Meester, statistics professor at TU Delft, an analytical expression was derived for the expected value of the coherence when the excitation and emission rates are equal (see below). This result is then used to find a formula that is valid for all rate parameters.

Equal Rates

Consider the case where the excitation rate and the emission rate are equal. Let $k_{ex} = k_{em} \equiv \lambda$, such that the intervals between emitted photons are distributed as $\mathrm{Exp}(\lambda) + \mathrm{Exp}(\lambda)$. The photon stream can then be described as a Poisson process with rate λ, where every second event is a photon. This process is used to define the distribution of X_i, the photon count in bin i from one emitter. Using X_i, the distribution of the total photon count in bin i, C_i, can be determined.

Three sequences have to be defined to describe X_i with a Poisson process. First, let $Y_1, ..., Y_m$ denote the numbers of Poisson events per bin so that Y_i is distributed as $\mathrm{Pois}(\lambda\Delta t)$. Second, U_i indicates the parity of Y_i, and thus, $U_i = N_i \mod 2$. Third, $B_0, ..., B_m$ is defined such that $B_i = 1$ indicates that the last Poisson event in bin i is a photon and $B_i = 0$ otherwise. This sequence is initialized with B_0, which is distributed as $\mathrm{Ber}(\frac{1}{2})$ so that the process is stationary.

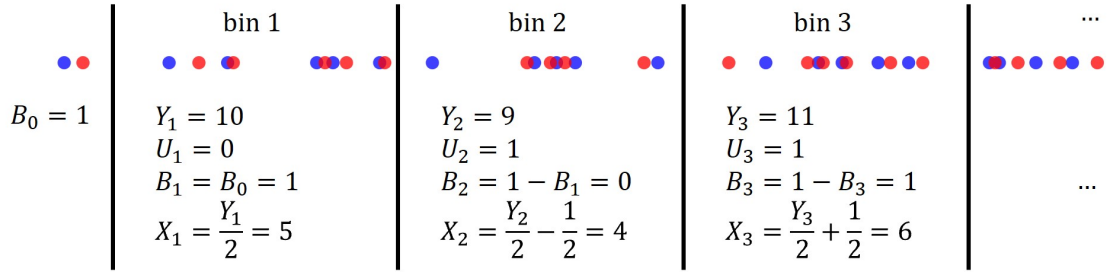

Figure 9: An example of how X_i can be described using a Poisson process. The dots represent Poisson-distributed events. Each red dot indicates a photon, while the blue dots are intermediate events. Three situations can be distinguished. **Bin 1:** the number of events Y_1 is even. **Bin 2:** Y_2 is odd, and the last event in the preceding bin is a photon ($B_1 = 1$). **Bin 3:** Y_3 is odd, and the last event in the preceding bin is not a photon ($B_2 = 0$).

Using these definitions, X_i can be defined in terms of Y_i, U_i, and B_i. As is shown in fig. 9, three situations can be distinguished. If Y_i is even, $X_i = Y_i/2$ and $B_i = B_{i-1}$. Otherwise, when Y_i is odd and $B_{i-1} = 0$, then $X_i = (Y_i + 1)/2$ and $B_i = 1$. The last possibility is that Y_i is odd and $B_{i-1} = 1$, in which case $X_i = (Y_i - 1)/2$ and $B_i = 0$. This can be combined into one equation as

$$X_i = \frac{Y_i}{2} + U_i\left(B_{i-1} - \frac{1}{2}\right), \quad B_i = \begin{cases} 1 - B_{i-1} & \text{if } U_i = 1 \\ B_{i-1} & \text{otherwise.} \end{cases} \tag{3.9}$$

Next, the expected value of X_i and X_i^2 can be calculated. The average value of X_i is $\mathbb{E}[X_i] = \mathbb{E}\left[\frac{1}{2}Y_i + U_i(B_{i-1} - \frac{1}{2})\right]$. Note that B_{i-1} is independent of Y_i and U_i, because it is only determined by B_0 and $Y_1, ..., Y_{i-1}$. Hence, the mean value of X_i is $\mathbb{E}[X_i] = \frac{1}{2}\mathbb{E}[Y_i] + \mathbb{E}[U_i] \cdot 0 = \frac{1}{2}\mathbb{E}[Y_i]$. To calculate the expected value of X_i^2 it is useful to condition on Y_i, which gives

$$\begin{aligned} \mathbb{E}\left[X_i^2|Y_i\right] &= \mathbb{E}\left[\frac{Y_i^2}{4} + Y_iU_i\left(B_{i-1} - \frac{1}{2}\right) + U_i^2\left(B_{i-1} - \frac{1}{2}\right)^2 \middle| Y_i\right] \\ &= \frac{Y_i^2}{4} + Y_iU_i\mathbb{E}\left[B_{i-1} - \frac{1}{2}\right] + U_i^2\mathbb{E}\left[\left(B_{i-1} - \frac{1}{2}\right)^2\right] \\ &= \frac{Y_i^2}{4} + 0 + U_i^2\mathbb{E}\left[B_{i-1}^2 - B_{i-1} + \frac{1}{4}\right] \\ &= \frac{Y_i^2}{4} + \frac{U_i^2}{4}. \end{aligned} \tag{3.10}$$

Using the law of total expectation, the expected value of X_i^2 is found to be

$$\mathbb{E}\left[X_i^2\right] = \frac{1}{4}\left(\mathbb{E}\left[Y_i^2\right] + \mathbb{E}\left[U_i^2\right]\right). \tag{3.11}$$

Now, multiple emitters are considered to determine $\mathbb{E}\left[C_i^2\right]$. Let X_{ij} denote the photon counts in bin i from emitter j so that $C_i = \sum_{j=1}^{m} X_{ij}$. Note that all emitters are independent and so $\mathbb{E}[X_{ij}X_{ik}] = \mathbb{E}[X_{ij}]\mathbb{E}[X_{ik}]$ when $j \neq k$. It then follows that

$$\begin{aligned} \mathbb{E}\left[C_i^2\right] &= \mathbb{E}\left[\left(\sum_{j=1}^{n} X_{ij}\right)^2\right] \\ &= \mathbb{E}\left[\sum_{j=1}^{n} X_{ij}^2\right] + \mathbb{E}\left[\sum_{j\neq k} X_{ij}X_{ik}\right] \\ &= n\mathbb{E}[X_i^2] + n(n-1)\mathbb{E}[X_i]^2 \\ &= \frac{n}{4}\mathbb{E}[Y_i^2] + \frac{n}{4}\mathbb{E}[U_i^2] + \frac{n^2}{4}\mathbb{E}[Y_i]^2 - \frac{n}{4}\mathbb{E}[Y_i]^2 \\ &= \frac{n}{4}\left(\mathrm{Var}(Y_i) + \mathbb{E}[U_i^2]\right) + \frac{n^2}{4}\mathbb{E}[Y_i]^2. \end{aligned} \tag{3.12}$$

The variance and expected value of Y_i are known from the basic properties of the Poisson distribution, $\mathrm{Var}(Y_i) = \mathbb{E}[Y_i] = \lambda\Delta t$. Furthermore, U_i is a $\mathrm{Ber}(\bar{p})$ random variable that is driven by Y_i, where $\bar{p}$ equals the probability that Y_i is odd. Thus, $\mathbb{E}[U_i^2] = \bar{p}$, for which $\bar{p}$ equals

$$\begin{aligned}\bar{p} &= \sum_{k=0}^{\infty} \frac{(\lambda\Delta t)^{2k+1} e^{-\lambda\Delta t}}{(2k+1)!} \\ &= \frac{1}{2}\left(1 - e^{-2\lambda\Delta t}\right).\end{aligned} \tag{3.13}$$

Substituting the expressions for $\mathbb{E}[Y_i^2]$ and $\mathbb{E}[U_i^2]$ in eq. (3.12) gives

$$\mathbb{E}\left[C_i^2\right] = \frac{n}{4}\left(n(\lambda\Delta t)^2 + \lambda\Delta t + \frac{1}{2}\left(1 - e^{-2\lambda\Delta t}\right)\right). \tag{3.14}$$

Finally, the expected value of the coherence is found by substituting eq. (3.14) into eq. (3.8). Using that $\mathbb{E}[N] = n \cdot \frac{1}{2}\lambda\Delta t m$, the expression simplifies to

$$\mathbb{E}\left[g^{(2)}[0]\right] = 1 - \frac{1}{n}\frac{1}{\lambda\Delta t}\left(1 - \frac{1 - e^{-2\lambda\Delta t}}{2\lambda\Delta t}\right). \tag{3.15}$$

To validate this formula, the results are compared to the outcomes of simulations. Figure 10a shows $g^{(2)}[0]$ for 1 to 4 fluorophores for which the rate parameters were equal ($k_{ex} = k_{em} = 1\ \mathrm{ns}^{-1}$). The analytical solution is indicated by the dashed line, and the semi-transparent area represents the average of 100 simulations together with one standard deviation on both sides ($\mu \pm 1\sigma$). As can be seen, the variance of the simulations is very small and the results align well with the analytical solution.

Unequal Rates

When $k_{ex} \neq k_{em}$, it is more complicated to derive the expected value of the coherence. It is not possible to use a Poisson process to describe the photon stream, since the intervals are distributed hypoexponentially. Therefore, instead of deriving a new equation, the result for equal rates (eq. (3.15)) is adjusted empirically to obtain a general formula that works for every set of (k_{ex}, k_{em}).

To modify the equation, note that eq. (3.15) contains an exponential term that is raised to the power $-2\lambda\Delta t$. This term can be recognized from eq. (3.6), in which $e^{-2\lambda\tau}$ appears, and for which it is known that the general equation is written as $e^{-(k_{ex}+k_{em})\tau}$. A logical step is thus to assume that $\lambda = \frac{1}{2}(k_{ex} + k_{em}) = \frac{1}{2}k$. Substituting this into eq. (3.15) gives

$$\mathbb{E}\left[g^{(2)}[0]\right] = 1 - \frac{1}{n}\frac{2}{k\Delta t}\left(1 - \frac{1 - e^{-k\Delta t}}{k\Delta t}\right). \tag{3.16}$$

This result is compared to simulations for different sets of rate parameters (fig. 10b-d). In fig. 10b, the sum of the rates is $k = 2\ \mathrm{ns}^{-1}$, and therefore, the graph is the same as in fig. 10a. Note that the measurement time for fig. 10b was increased to 62.5 ms to reduce the variance. In fig. 10c and fig. 10d, k is 6 and 51 ns^{-1}, respectively, resulting in a steeper incline. Figure 10d shows a slightly larger variance, which is because Δt is large compared to k. As the figures show, eq. (3.16) correctly describes the coherence for all parameter sets.

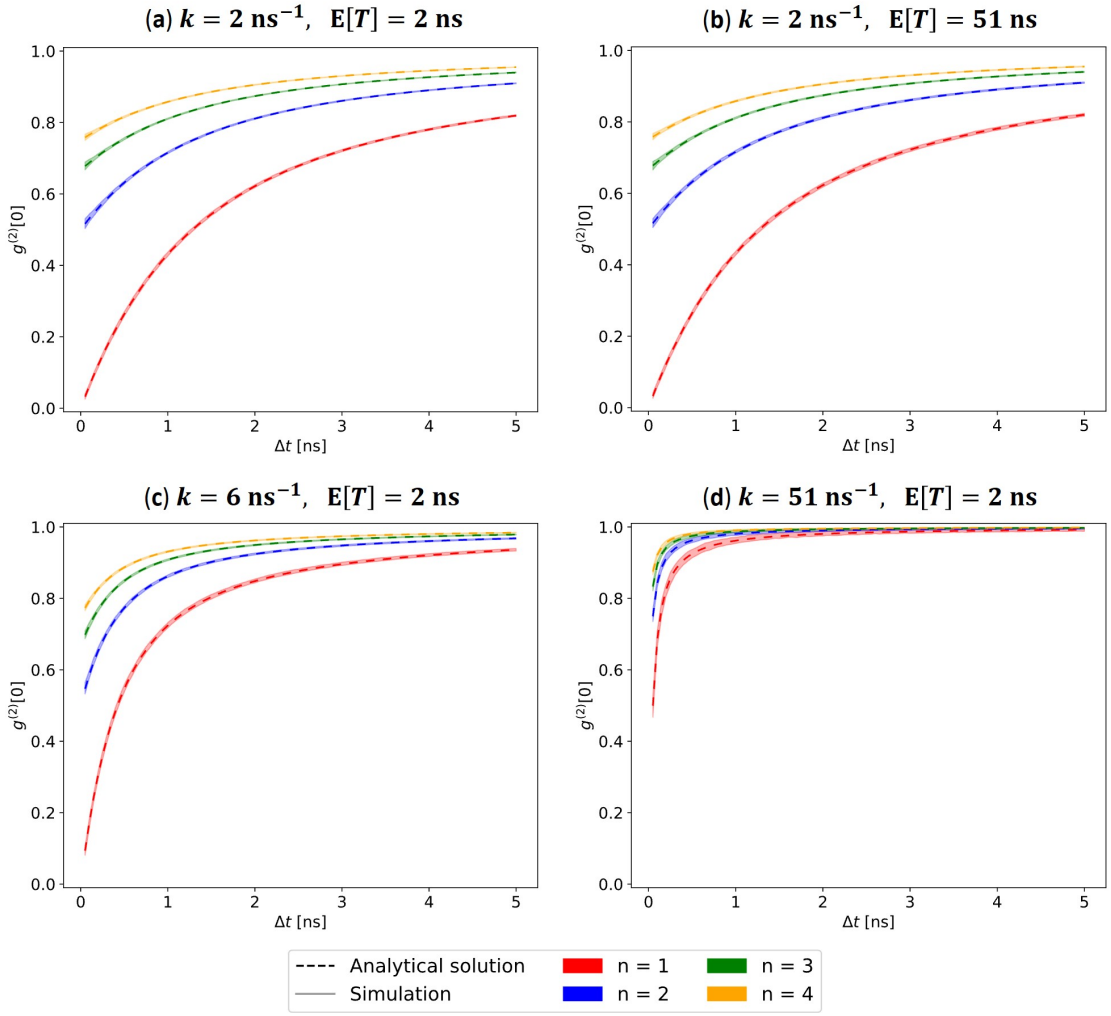

Figure 10: The second-order coherence at $\ell\Delta t = 0$ increases with the bin size Δt and the sum of rates k. The dashed line indicates the analytical solution from eq. (3.16) and the semi-transparent area represents the average value of 100 simulations with a 1σ interval. (**a**) Equal rate parameters of $k_{ex} = k_{em} = 1\ \mathrm{ns}^{-1}$ give the least amount of variance. (**b**) $g^{(2)}[0]$ is independent of $\mathbb{E}[T]$. (**c - d**) As k increases, $g^{(2)}[0]$ becomes more biased towards 1.

3.2 Estimation of the Number of Emitters

Using the result of the previous section, the number of emitters can be written as a function of $k = k_{ex} + k_{em}$ and the bin size Δt. Rearranging eq. (3.16) gives

$$n(k\Delta t) = \frac{f(k\Delta t)}{1 - g^{(2)}[0]}, \quad f(k\Delta t) = \frac{2}{k\Delta t}\left(1 - \frac{1 - e^{-k\Delta t}}{k\Delta t}\right), \tag{3.17}$$

where $g^{(2)}[0]$ is the value of the coherence at $\ell = 0$.

Using the same conditions as for the simulations from fig. 10, fig. 11 shows the average value of n that was calculated with eq. (3.17), together with the 1σ interval of the simulations. The variance that is found for n varies linearly with the uncertainty of the coherence. In fig. 11a-c it can be seen that the standard deviation σ is larger when the bin size is very small. This is because the data is sparser with a smaller bin size, resulting in a larger variance between the simulations. The standard error slightly increases for large Δt, mostly because the number of bins in the measurement interval decreases when the bin size increases. Therefore, the number of data points is smaller, which results in a higher variance.

Figure 11d stands out because the standard error of n is high. The reason for this is that k is much larger than in the other examples, and thus, $g^{(2)}[0]$ converges to 1 quickly. When $g^{(2)}[0] \approx 1$, a small deviation in the coherence leads to a large deviation in n. Furthermore, $g^{(2)}[0]$ occasionally rises above 1, which results in $n \ll 0$. Therefore, the standard deviation of n is very high. As can

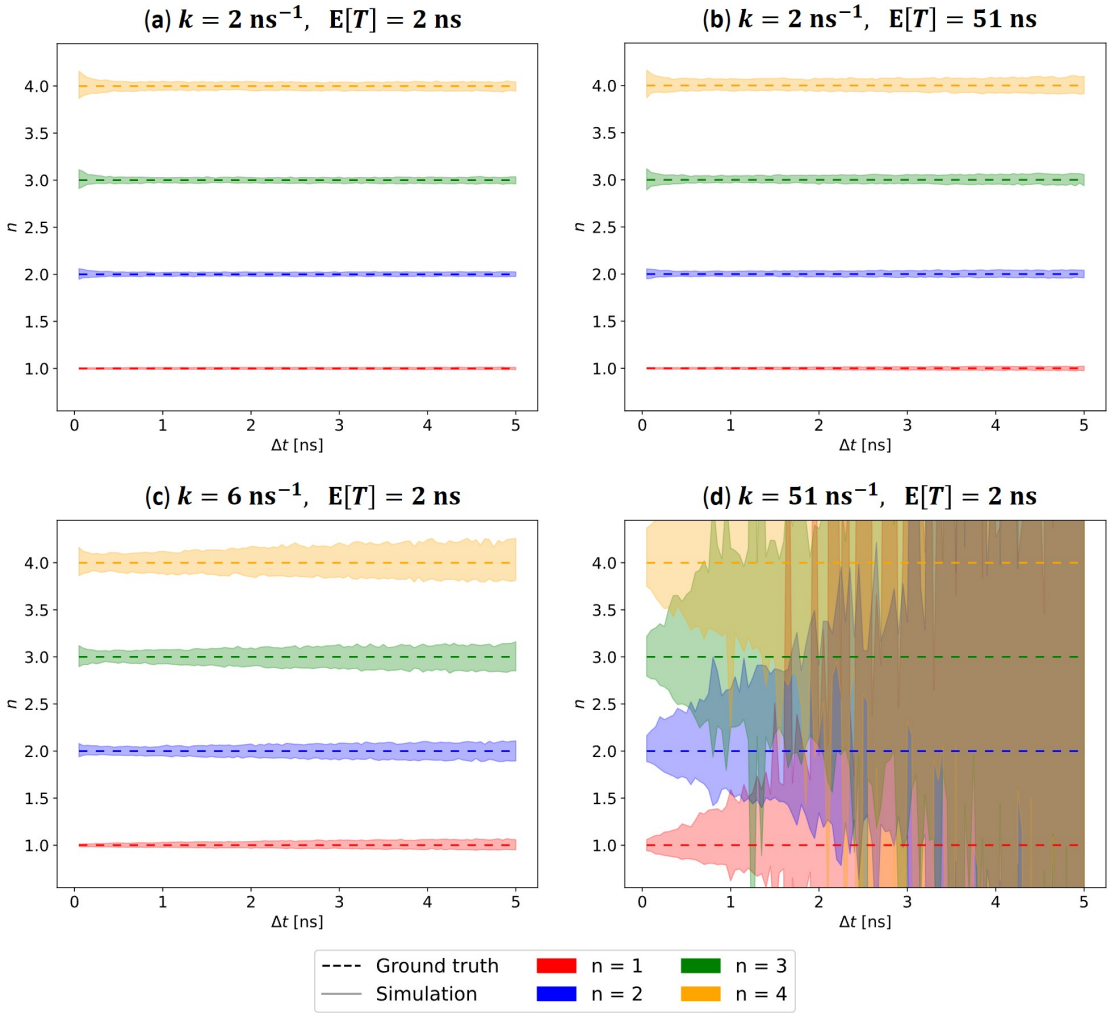

Figure 11: (**a** - **d**) For each simulation of fig. 10a-d, the number of emitters is calculated using eq. (3.17). The semi-transparent area represents the average value of 100 simulation results with a 1σ interval.

be seen in the figure, σ decreases for smaller bin sizes, which indicates that a bin size in the order of 0.001 ns could give better results, as was used before in fig. 6b.

Looking at fig. 11, there seems to be an optimal bin size for each set of parameters, for which the standard deviation of n is minimal. This is shown the most clearly in fig. 11c around the line for which $n = 4$, where the spread first decreases to a minimum and then increases. To estimate the optimal bin size, the variance of $g^{(2)}[0]$ is determined analytically. A detailed derivation is provided in appendix B. The standard deviation of n (σ_n) depends linearly on the standard deviation of the second-order quantum coherence at lag 0 (σ_g). This can be shown by applying error propagation to eq. (3.17), writing σ_n as

$$\sigma_n = \left|\frac{\partial n}{\partial g^{(2)}[0]}\right| \sigma_g = \frac{f(k\Delta t)}{(1 - g^{(2)}[0])^2}\sigma_g = \frac{n^2}{f(k\Delta t)}\sigma_g. \tag{3.18}$$

Figure 12a,c shows the standard deviations σ_g and σ_n that were found in the simulations of fig. 10a and fig. 11a, respectively. In these simulations, the rate parameters were $k_{ex} = k_{em} = 1$ ns^{-1} so that $k = 2$ ns^{-1} and $\mathbb{E}[T] = 2$ ns. The dashed lines indicate the analytical result for comparison. Similarly, fig. 12b,d shows the errors found in the simulations of fig. 10c and fig. 11c, for which $k_{ex} = 0.55$ and $k_{em} = 5.5$ ns^{-1} so that $k = 6$ ns^{-1} and $\mathbb{E}[T] = 2$ ns. As can be seen, the simulation outcomes have different magnitudes than the analytical solution, but they generally show the same behavior. The difference between the graphs is likely due to a mistake in the derivation of σ_g since it is lengthy and prone to errors. Nevertheless, the minima of the analytical solution in fig. 12c,d exactly match the bin size for which the standard error of the simulation is smallest. Therefore, the analytical solution can be used to determine the optimal bin size to obtain the most accurate estimate of the emitter count.

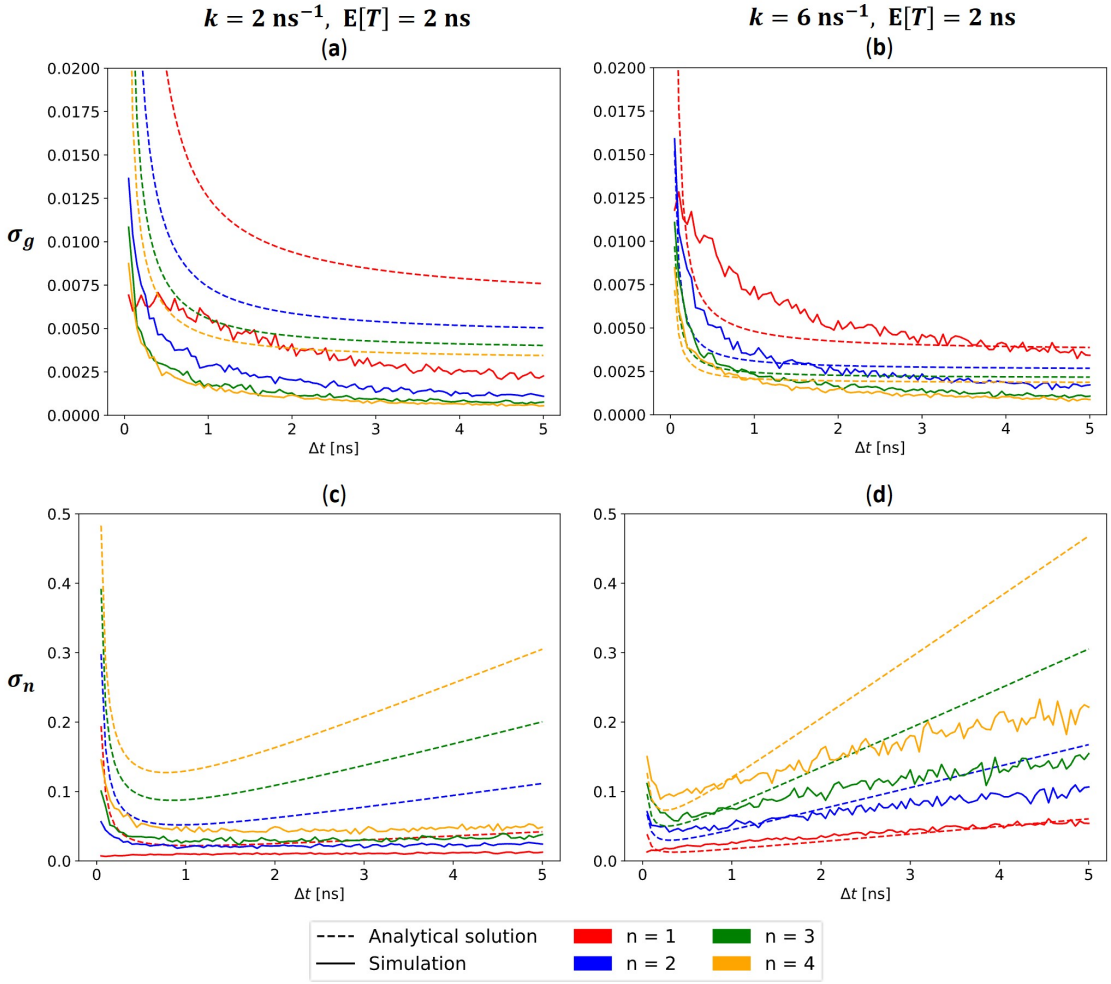

Figure 12: Comparison of standard deviations found from 100 simulations (solid line) and derived analytically (dashed line) for $k = 2$ ns^{-1} (**a**, **c**) and $k = 6$ ns^{-1} (**b**, **d**), and expected photon intervals of $\mathbb{E}[T] = 2$ ns. Although the magnitudes of the graphs do not match, the curves show comparable behavior. (**a**, **b**) The standard deviation of $g^{(2)}[0]$ (σ_g). (**c**, **d**) The standard deviation of n (σ_n). The dip in the analytical solution coincides with the bin size that gives minimal variance in the simulations.

3.2.1 Many Emitters

So far, only 1 to 4 fluorophores were considered. To assess the performance for higher numbers of molecules, simulations were run for up to $n = 100$ emitters for the best-case scenario in the case that the measurement time is $\mathcal{T}_0 = 0.1$ ms and the fluorescent dye is Alexa647 with $\tau_l = 1$ ns. To obtain a minimal error, the rate parameters were equal ($k_{ex} = k_{em} = 1$ ns^{-1}) and the bin size was 1 ns. As can be seen in fig. 12c, this is approximately the bin size for which the standard deviation of n is the smallest.

Figure 13a shows the average value of n that was found from 100 simulations with an error bar of size $1\sigma_n$. The horizontal axis shows the true number of emitters, n_0. As the figure shows, the results are very accurate for the entire range of n_0. From fig. 13b and fig. 13c it can be seen that the standard error increases linearly with the number of emitters and that it has an average value of 0.01. The number of fluorophores can thus be estimated with an uncertainty of $0.01n_0$.

The same simulations were repeated for shorter measurement times. When the measurement interval is 0.01 ms, the number of emitters can be determined with a standard error of 4%, and when $\mathcal{T} = 0.001$ ms, the standard error is $0.1n_0$. For different rates and detection efficiencies, the required measurement time to achieve these standard errors can be calculated using the results from section 3.1.2.

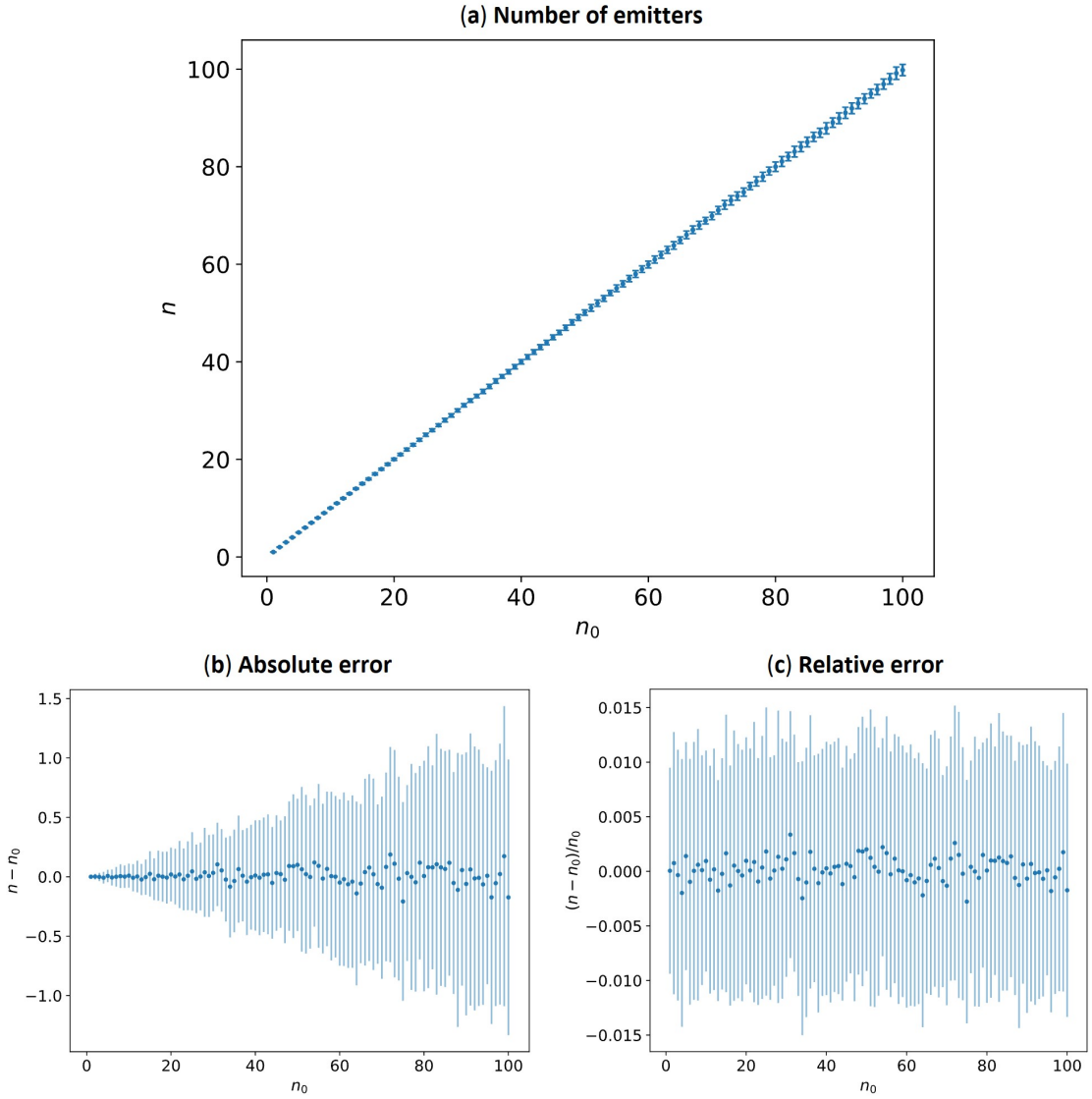

Figure 13: (**a**) The number of emitters n was estimated for $1 \leq n_0 \leq 100$, using $k = 2$ ns^{-1}, $\mathbb{E}[T] = 2$ ns and $\Delta t = 1$ ns. The standard deviation σ_n increases with $0.01n_0$. (**b**) The absolute error $n - n_0$ with a $1\sigma_n$-interval. (**c**) The relative error $(n - n_0)/n_0$ with a $1\sigma_n/n_0$ interval.

4. Discussion

4.1 Main results

The discrete-time second-order quantum coherence can be calculated from photon arrival times measured by a SPAD array. The resulting curve shows that the fluorescent molecules emit anti-bunched light. When the excitation and emission rates of the molecules are equal, the antibunching effect is strongest because the photon intervals are the most regular. As a result, the variance of the measured coherence is minimal.

However, to achieve an excitation rate that matches the emission rate of Alexa647, a laser with a power of 10^2 kWcm^{-2} is required, which can cause damage to the sample. Therefore, in experimental settings lower intensities in the order of 10 kWcm^{-2} are preferred, so that the excitation rate is lower, whereas the emission rate of the molecules remains unchanged as that is a property of the fluorescent dye. Consequently, the average photon interval time is much longer than before. Since the excitation and emission rates are not equal in this case, the antibunching effect is less strong, which can be observed from an increased variance in the coherence.

Results showed that the variance of the second-order quantum coherence can be reduced by prolonging the measurement interval. When the variance of one process is known, the measurement time that is required to obtain the same variance with another process can be calculated using the two following rules. Firstly, consider two processes a and b for which the sum of rates is equal ($k_a = k_b$) but the excitation and emission rates differ. The expected interval times then differ by a constant α so that $\mathbb{E}[T_a] = \alpha\mathbb{E}[T_b]$. To obtain the same variance in the coherence for both processes, it was shown that the measurement times should equal $\mathcal{T}_a = \alpha^2\mathcal{T}_b$ (fig. 7). Secondly, it is possible to compare two processes for which the sum of rates differs ($k_a \neq k_b$) when they both have equal rate parameters: $k_{ex,a} = k_{em,a}$ and $k_{ex,b} = k_{em,b}$. If $k_a = \beta^{-1}k_b$ so that $\mathbb{E}[T_a] = \beta\mathbb{E}[T_b]$, the variance of the coherence is equal for both processes when $\mathcal{T}_a = \beta\mathcal{T}_b$ since all experimental parameters are scaled linearly by a factor β. Using these rules, all combinations of rate parameters can be compared to each other.

Nevertheless, increasing the measurement time is not always possible, as it is an important limiting factor for dynamic imaging. Although it may seem counterintuitive, using a fluorophore with a longer lifetime can help to reduce the measurement time, provided that it makes the excitation and emission rate more equal. Considering the aforementioned calculation rules, the measurement interval will increase more linearly than quadratically when the rate parameters are approximately equal. Physically, this can be understood by observing that the photon intervals are more regular when the difference between the rate parameters is minimal, causing a strong antibunching effect so that fewer photons are needed to obtain accurate results.

Furthermore, it was shown that the detection efficiency does not limit the accuracy of the coherence (fig. 8). When the detection efficiency is less than 100%, which is always the case for experimental setups, increasing the measurement time can compensate for the lack of detection efficiency. Comparing two processes with $k_a = k_b$ and $\eta_a\mathbb{E}[T_a] = \eta_b\mathbb{E}[T_b]$, then $\eta_a^2\mathcal{T}_a = \eta_b^2\mathcal{T}_b$ gives equal variance for both. Thus, the detection efficiency is not a limiting factor for the accuracy of the coherence, except when the required measurement time is too long for the specific application, which is a promising result for further research.

This research focused on determining the number of fluorophores in an ROI, which is directly related to the second-order quantum coherence at time lag 0. However, the discretization of the coherence introduces a bias since every bin carries information about a small interval, instead of a point in time. This deviation can be described analytically as a function of the fluorescent dye's summed excitation and emission rates, and the bin size (eq. (3.16), fig. 10). By correcting for this bias, the number of Alexa647 emitters can be determined with a relative error of 0.01 from a 0.1 ms measurement in the most optimal case, meaning that the rate parameters are equal ($k_{ex} = k_{em}$) and the detection efficiency is 100% (eq. (3.17), fig. 13).

In practice, a longer measurement time is needed to obtain this accuracy. Realistic experimental parameters for an Alexa647-dyed sample ($k_{em} = 1$ ns^{-1}) are a laser intensity of 10 kWcm^{-2} ($k_{ex} = 0.03$ ns^{-1}) and 10% detection efficiency. The sum of rates is then $k = 1.03$ ns^{-1} and the expected interval time is 343 ns. Consequently, the required measurement time to obtain a 0.01 relative error is 1515 ms, which is relatively long. The measurement interval can be shortened by using a fluorophore with a longer lifetime but absorption coefficient and wavelength comparable to Alexa647. For example, a dye with the same properties as Alexa647, but with a 2 ns lifetime would only require an 826 ms measurement, decreasing the interval by almost 50%. If the detection efficiency could be improved by 1%, this would reduce the measurement interval by almost 20% to 1252 ms. Naturally, the measurement time can be shortened when a larger error is acceptable. It was shown that the relative error increases to approximately 0.04 when the measurement time is reduced by 90%, and to 0.1 when it is shortened to 1% of the original time.

It was found that the standard deviation of the emitter count depends on the bin size chosen for the discretization of the signal. When the bin size goes to zero, the variance explodes because the signal is too sparse to obtain a reliable result from the second-order quantum coherence. After decreasing to a minimum, the variance gradually increases for large bin sizes. This can be largely attributed to the reduced number of bins that fit in an interval when the bin size is large, giving a less precise result for the coherence as it is calculated from fewer data points. At the minimum, the sparsity of the signal and the number of bins are optimally balanced, resulting in a high accuracy. The bin size for which the variance is minimal can be located using an analytical formula. In practice, the bin size is bounded by the timing accuracy of the SPAD array. Given the specifications of current sensors, the bin size has to be at least 0.35 ns. This value will likely be even larger in experimental settings. As the optimal bin size decreases as the sum of rates k increases, it is important to choose k small enough such that the optimal bin size exceeds the minimal bin size.

4.2 Limitations

An important limitation of this research is that all fluorophores were assumed to emit photons at the same constant rate. This is generally not the case in experiments. The emission and excitation rates can differ locally due to a non-uniform laser power at the sample or due to local circumstances that affect the absorption cross-section or lifetime of the fluorophores. Simulations empirically showed that fluctuations up to 50% of the lifetime and/or the laser intensity have negligible effects on the second-order quantum coherence at time lag 0 when the bin size is small compared to the sum of rates k. As a function of the time lag, the coherence converges to 1 faster for fluorophores with varying rate parameters than for emitters with equal properties. Consequently, the coherence at lag 0 is more biased towards 1 than expected for bigger bin sizes, leading to an overestimation of the number of emitters.

In addition, it was assumed that every excitation leads to the emission of a fluorescence photon. Thus, decay to a triplet state and non-radiative decay were neglected. When an emitter decays via the triplet state or through non-radiative decay, it is invisible during the process. As the average lifetime of these processes is several orders longer than for fluorescence, this influences the average rate of the emitter significantly, and it was empirically observed that this impacts the coherence substantially. Moreover, if the decay period covers the entire measurement interval, the fluorophore remains invisible in that frame. Further research is needed to quantify the effect of these processes. To minimize the impact on the results, it is favorable to use a fluorescent dye with a high quantum yield.

Moreover, no sources of noise were considered in this thesis. Background noise and dark counts will likely bias the coherence towards 1 as more photon pairs are found, resulting in an overestimation of the true number of emitters. When the average background and dark count rates are known, the data can likely be corrected for these noise sources.

Another topic that requires further research is the influence of the dead time of the SPAD sensor, which was taken to be zero in this thesis. Per definition, the dead time makes it impossible to simultaneously detect photons on one pixel, while this simultaneousness provides valuable information about the sample. The measurements are least affected by the dead time if it is much shorter than the average photon interval, and when the excitation and emission rates are approximately equal since this results in the most regular spacing between the photons. When the fluorophore density is high, more photons rapidly succeed each other and more photons will not be detected. Therefore, SPAD sensors with a nanosecond or even sub-nanosecond dead time are strongly preferred. Given the rapid development of SPAD arrays in the last decades, it can be

expected that these will soon be available. Another option is to split the emission beam on multiple SPAD detectors by adding one or several beam splitters. However, this is financially unattractive because of the high costs of SPAD sensors. Moreover, practical difficulties in the setup might lead to a reduced localization and timing accuracy.

Although a short dead time benefits photon detection, it generally increases the after-pulsing probability. To prepare for a new detection, the photon avalanche within the detector must be quenched, and the SPAD pixel has to be reset to the initial conditions. If this process is shortened maximally, the probability increases of an avalanche charge remaining in the SPAD, which causes after-pulsing. An after-pulsing event results in both a dark count, as another period of dead time, which means that the apparent dead time doubles. Thus, while the SPAD array should have a short dead time, it is also important that it has a reasonable after-pulsing probability.

Another trade-off is between the crosstalk probability and the fill factor of the SPAD array. When the pixels of the detector are placed closer together, more area is covered and therefore, the detection efficiency improves. However, that also facilitates electroluminescence photons to reach a neighboring pixel and cause a dark count. As a longer measurement time can compensate for a lower detection efficiency, choosing a detector with low crosstalk probabilities might be preferable.

4.3 Outlook

The next step is to develop an SMLM algorithm for SPAD data. Whereas conventionally the measured intensity is the only source of information, a SPAD SMLM algorithm has extra knowledge about the number of fluorescent molecules. One possibility is to use the emitter count as an input for multi-emitter fitting[7]. Another option is to obtain an initial estimate of the fluorophore positions from second-order quantum coherence and then use the intensity to localize the emitters precisely.

Several methods were explored to estimate the emitter positions using the coherence. The second-order quantum coherence was calculated per pixel for a 3x3 kernel centered at that pixel so that the resulting value indicates how many emitters contributed to the signal in that neighborhood. This information was then used to create an emitter map, which was subsequently overlaid with the measured intensity. Figure 14 shows an example of the intensity of 30 fluorophores on a 15x15 sensor, giving a density of 4.82 μm^{-2}, and in fig. 14b, the corresponding emitter map is shown. Various techniques were applied to this map to estimate the fluorophore locations, including deconvolution, Wiener filtering, k-means clustering, and applying an inverse morphology operation. However, none of these yielded promising results. An explanation for this is that every pixel measures different fractions of the PSFs of multiple emitters. Most fluorophores are therefore counted multiple times at different pixels, complicating the puzzle. The solution to this puzzle will be the first step in developing a specialized SMLM algorithm for SPAD arrays.

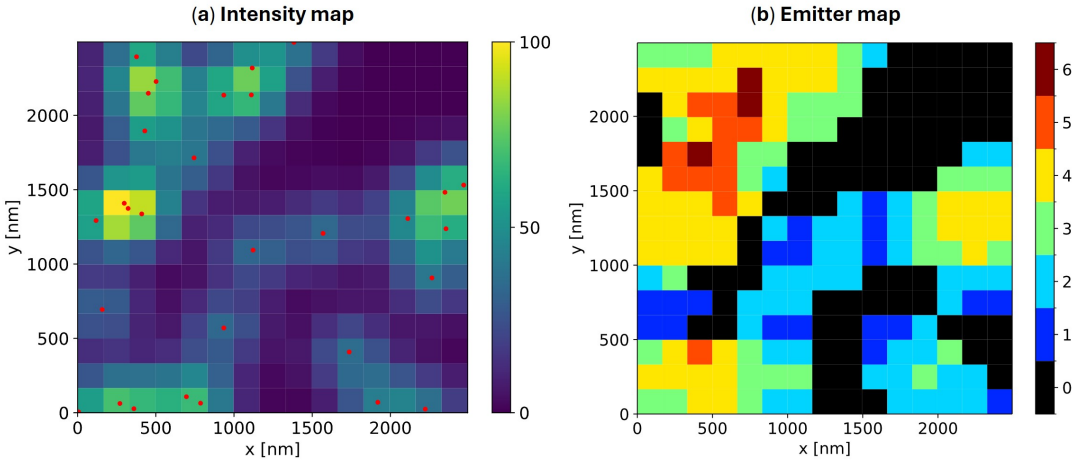

Figure 14: (**a**) The normalized intensity per pixel in a 0.1 ms simulation of 30 Alexa647 fluorophores. The red dots indicate the ground truth locations of the emitters. (**b**) The emitter map shows the number of emitters that contributed to a 3x3 neighborhood centered at each pixel.

5. Conclusion

This research explored the possibilities of using a SPAD array for SMLM measurements. An analytical expression was derived to determine the number of fluorophores from simulated SPAD measurements. From a 0.1 ms measurement, the number of Alexa647 fluorophores can be determined with a standard error of 1% independent of the number of emitters, assuming equal excitation and emission rates and 100% detection efficiency. Although higher standard deviations are found when the rate parameters are unequal or when the detection efficiency is low, the loss of accuracy can be fully compensated for by prolonging the measurement interval. Considering a laser intensity of 10 kWcm^{-2} and a 10% detection efficiency, a measurement of 1.5 s is needed to obtain a standard error of 1%, whereas a 15 ms measurement results in a 10% error. Further research is needed to establish the effects of background noise, dark counts, and the dead time of the SPAD array on the accuracy of the results.

The results of this thesis show great potential for single-molecule localization microscopy. The newly acquired information about the number of emitters helps to locate fluorophores with overlapping point spread functions for multi-emitter fitting. Consequently, SPAD arrays will provide the ability to image high emitter densities, which enables faster data acquisition and dynamic imaging.

Bibliography

[1] M. Sauer and M. Heilemann, "Single-molecule localization microscopy in eukaryotes," *Chemical Reviews*, vol. 117, no. 11, pp. 7478–7509, Mar. 2017. DOI: 10.1021/acs.chemrev.6b00667.

[2] M. Lelek, M. T. Gyparaki, G. Beliu, F. Schueder, J. Griffié, *et al.*, "Single-molecule localization microscopy," *Nature Reviews Methods Primers*, vol. 1, no. 1, p. 39, Jun. 2021. DOI: 10.1038/s43586-021-00038-x.

[3] C. Smith, M. Huisman, M. Siemons, D. Grünwald, and S. Stallinga, "Simultaneous measurement of emission color and 3D position of single molecules," *Optics Express*, vol. 24, no. 5, pp. 4996–5013, Feb. 2016. DOI: 10.1364/OE.24.004996.

[4] S. Van De Linde, S. Wolter, M. Heilemann, and M. Sauer, "The effect of photoswitching kinetics and labeling densities on super-resolution fluorescence imaging," *Journal of Biotechnology*, vol. 149, no. 4, pp. 260–266, Sep. 2010. DOI: 10.1016/j.jbiotec.2010.02.010.

[5] A. Speiser, L. R. Müller, P. Hoess, U. Matti, C. J. Obara, *et al.*, "Deep learning enables fast and dense single-molecule localization with high accuracy," *Nature Methods*, vol. 18, no. 9, pp. 1082–1090, Sep. 2021. DOI: 10.1038/S41592-021-01236-X.

[6] H. Li and J. C. Vaughan, "Switchable fluorophores for single-molecule localization microscopy," *Chemical Reviews*, vol. 118, no. 18, pp. 9412–9454, Sep. 2018. DOI: 10.1021/acs.chemrev.7b00767.

[7] F. Huang, S. L. Schwartz, J. M. Byars, K. A. Lidke, B. Huang, *et al.*, "Simultaneous multiple-emitter fitting for single molecule super-resolution imaging," *Biomedical Optics Express*, vol. 2, no. 5, pp. 1377–1393, Apr. 2011. DOI: 10.1364/BOE.2.001377.

[8] S. Cox, E. Rosten, J. Monypenny, T. Jovanovic-Talisman, D. T. Burnette, *et al.*, "Bayesian localization microscopy reveals nanoscale podosome dynamics," *Nature Methods*, vol. 9, no. 2, pp. 195–200, Dec. 2011. DOI: 10.1038/NMETH.1812.

[9] M. Pawlowska, R. Tenne, B. Ghosh, A. Makowski, and R. Lapkiewicz, "Embracing the uncertainty: The evolution of SOFI into a diverse family of fluctuation-based super-resolution microscopy methods," *Journal of Physics: Photonics*, vol. 4, no. 1, p. 012 002, Jan. 2022. DOI: 10.1088/2515-7647/ac3838.

[10] J. Min, C. Vonesch, H. Kirshner, L. Carlini, N. Olivier, *et al.*, "FALCON: Fast and unbiased reconstruction of high-density super-resolution microscopy data," *Scientific Reports*, vol. 4, no. 1, p. 4577, Apr. 2014. DOI: 10.1038/SREP04577.

[11] D. Sage, H. Kirshner, T. Pengo, N. Stuurman, J. Min, *et al.*, "Quantitative evaluation of software packages for single-molecule localization microscopy," *Nature Methods*, vol. 12, no. 8, pp. 717–724, Jun. 2015. DOI: 10.1038/NMETH.3442.

[12] D. Sage, T. A. Pham, H. Babcock, T. Lukes, T. Pengo, *et al.*, "Super-resolution fight club: Assessment of 2D and 3D single-molecule localization microscopy software," *Nature Methods*, vol. 16, no. 5, pp. 387–395, Apr. 2019. DOI: 10.1038/S41592-019-0364-4.

[13] C. Cabriel, T. Monfort, C. G. Specht, and I. Izeddin, "Event-based vision sensor for fast and dense single-molecule localization microscopy," *Nature Photonics*, vol. 17, no. 12, pp. 1105–1113, Oct. 2023. DOI: 10.1038/s41566-023-01308-8.

[14] I. Cusini, D. Berretta, E. Conca, A. Incoronato, F. Madonini, *et al.*, "Historical Perspectives, State of art and Research Trends of Single Photon Avalanche Diodes and Their Applications (Part 1: Single Pixels)," *Frontiers in Physics*, vol. 10, p. 906 675, Jun. 2022. DOI: 10.3389/FPHY.2022.906675.

[15] C. Bruschini, H. Homulle, I. M. Antolovic, S. Burri, and E. Charbon, "Single-photon avalanche diode imagers in biophotonics: Review and outlook," *Light: Science & Applications*, vol. 8, no. 1, p. 87, Sep. 2019. DOI: 10.1038/S41377-019-0191-5.

[16] F. Severini, I. Cusini, D. Berretta, K. Pasquinelli, A. Incoronato, and F. Villa, "SPAD pixel with sub-ns dead-time for high-count rate applications," *IEEE Journal of Selected Topics in Quantum Electronics*, vol. 28, no. 2, 2022. DOI: 10.1109/JSTQE.2021.3124825.

[17] PI Imaging. "SPAD23 Data Sheet." (Accessed on 22-05-2024), [Online]. Available: https://piimaging.com/datasheet/SPAD23datasheet.pdf.

[18] C. Bruschini, H. Homulle, and E. Charbon, "Ten years of biophotonics single-photon SPAD imager applications: Retrospective and outlook," in *Multiphoton Microscopy in the Biomedical Sciences XVII*, SPIE, vol. 10069, Feb. 2017, pp. 213–233. DOI: 10.1117/12.2256247.

[19] F. Zappa, A. Gulinatti, P. Maccagnani, S. Tisa, and S. Cova, "SPADA: Single-photon avalanche diode arrays," *IEEE Photonics Technology Letters*, vol. 17, no. 3, pp. 657–659, Mar. 2005. DOI: 10.1109/LPT.2004.840920.

[20] Teledyne Photometrics. "Kinetix sCMOS Camera." (Accessed on 22-05-2024), [Online]. Available: https://www.photometrics.com/products/kinetix-family/kinetix.

[21] A. Ficorella, L. Pancheri, G.-F. Dalla Betta, P. Brogi, G. Collazuol, *et al.*, "Crosstalk mapping in CMOS SPAD arrays," in *2016 46th European Solid-State Device Research Conference (ESSDERC)*, IEEE, Sep. 2016, pp. 101–104. DOI: 10.1109/ESSDERC.2016.7599598.

[22] I. M. Antolovic, S. Burri, C. Bruschini, R. Hoebe, and E. Charbon, "Analyzing blinking effects in super resolution localization microscopy with single-photon SPAD imagers," in *Single Molecule Spectroscopy and Superresolution Imaging IX*, SPIE, vol. 9714, Mar. 2016, p. 971 406. DOI: 10.1117/12.2211430.

[23] Q. Houwink, D. Kalisvaart, S.-T. Hung, J. Cnossen, D. Fan, *et al.*, "Theoretical minimum uncertainty of single-molecule localizations using a single-photon avalanche diode array," *Optics Express*, vol. 29, no. 24, pp. 39 920–39 929, Nov. 2021. DOI: 10.1364/OE.439340.

[24] I. Gyongy, A. Davies, N. A. Dutton, R. R. Duncan, C. Rickman, *et al.*, "Smart-aggregation imaging for single molecule localisation with SPAD cameras," *Scientific Reports*, vol. 6, no. 1, p. 37 349, Nov. 2016. DOI: 10.1038/SREP37349.

[25] Y. Israel, R. Tenne, D. Oron, and Y. Silberberg, "Quantum correlation enhanced super-resolution localization microscopy enabled by a fibre bundle camera," *Nature Communications*, vol. 8, no. 1, p. 14 786, Mar. 2017. DOI: 10.1038/NCOMMS14786.

[26] S. Stallinga and B. Rieger, "Accuracy of the Gaussian point spread function model in 2D localization microscopy," *Optics Express*, vol. 18, no. 24, pp. 24 461–24 476, Nov. 2010. DOI: 10.1364/OE.18.024461.

[27] B. Zhang, J. Zerubia, and J.-C. Olivo-Marin, "Gaussian approximations of fluorescence microscope point-spread function models," *Applied Optics*, vol. 46, no. 10, pp. 1819–1829, Apr. 2007. DOI: 10.1364/AO.46.001819.

[28] J. E. Berlier, A. Rothe, G. Buller, J. Bradford, D. R. Gray, *et al.*, "Quantitative comparison of long-wavelength Alexa Fluor dyes to Cy dyes: Fluorescence of the dyes and their bioconjugate," *Journal of Histochemistry & Cytochemistry*, vol. 51, no. 12, pp. 1699–1712, Dec. 2003. DOI: 10.1177/002215540305101214.

[29] J. R. Lakowicz, *Principles of Fluorescence Spectroscopy*, 3rd ed. Boston, MA: Springer US, 2006, pp. 58–59, ISBN: 978-0-387-31278-1. DOI: 10.1007/978-0-387-46312-4.

[30] P. Verdonck, *Advances in Biomedial Engineering*, 1st ed. Oxford: Elsevier, 2009, pp. 151–151, ISBN: 978-0-444-53075-2.

[31] C. Gerry and P. Knight, *Introductory Quantum Optics*. New York, NY: Cambridge University Press, 2005, ISBN: 978-0-521-82035-6. DOI: 10.1017/CBO9780511791239.

[32] S. C. Kitson, P. Jonsson, J. G. Rarity, and P. R. Tapster, "Intensity fluctuation spectroscopy of small numbers of dye molecules in a microcavity," *Physical Review A*, vol. 58, no. 1, p. 620, Jul. 1998. DOI: 10.1103/PhysRevA.58.620.

[33] K. S. Grußmayer and D.-P. Herten, "Photon antibunching in single molecule fluorescence spectroscopy," in *Advanced Photon Counting: Applications, Methods, Instrumentation*, P. Kapusta, M. Wahl, and R. Erdmann, Eds. Cham: Springer, 2014, vol. 15, pp. 159–190, ISBN: 978-3-319-15636-1. DOI: 10.1007/4243_2014_71.

A. Interval Distribution for Non-Ideal Detection Efficiency

The photon interval distribution changes when $\eta < 1$. Let A be the number of undetected photons between two detection events. A is a Geo(η) random variable, as every photon is detected with probability η. Now let $X_1, X_2, ...$ be distributed as Exp(k_{ex}) and $Y_1, Y_2, ... \sim$ Exp(k_{em}). The distribution of the new intervals T' can then be written as

$$T' = T'_{ex} + T'_{em} = \sum_{i=1}^{A} X_i + \sum_{i=1}^{A} Y_i, \tag{A.1}$$

where T'_{ex} and T'_{em} are the sum of A excitation and emission times, respectively. T'_{ex} is an Exp(ηk_{ex}) random variable and, likewise, $T'_{em} \sim$ Exp(ηk_{ex}). One could thus (wrongly) assume that $T' \sim$ Exp(ηk_{ex}) + Exp(ηk_{em}).

However, the distribution of T' actually approaches a Poisson distribution as η decreases. Since T'_{ex} and T'_{em} both consist of A terms, they are dependent variables. Using that $\mathbb{E}[T'_{ex}T'_{em}] = (2-\eta)/(\eta^2 k_{ex}k_{em})$ and using the properties of exponential variables, the correlation coefficient equals

$$\rho(T'_{ex}, T'_{em}) = \frac{\mathbb{E}[T'_{ex}T'_{ex}] - \mathbb{E}[T'_{ex}]\mathbb{E}[T'_{ex}]}{\sqrt{\mathrm{Var}(T'_{ex})\mathrm{Var}(T'_{em})}} = 1 - \eta. \tag{A.2}$$

Thus, their correlation increases as $\eta \to 0$. For a perfectly correlated signal where $\rho = 1$, it would mean that T'_{ex} and T'_{em} were generated from the same uniform $U(0,1)$ distribution. In that case,

$$T' = \frac{-\ln U}{\eta k_{ex}} + \frac{-\ln U}{\eta k_{em}} = \frac{-\ln U}{\left(\frac{\eta k_{ex}k_{em}}{k_{ex}+k_{em}}\right)} \tag{A.3}$$

so that

$$T' \sim \mathrm{Exp}\left(\left(\frac{1}{\eta k_{ex}} + \frac{1}{\eta k_{em}}\right)^{-1}\right), \tag{A.4}$$

meaning that the detection events would follow a Poisson distribution with rate $\eta(k_{ex}^{-1} + k_{em}^{-1})^{-1}$.

B. Variance of the Second-Order Quantum Coherence

B.1 Derivation

To determine the standard error for the number of emitters, the variance of the second-order quantum coherence at lag 0 needs to be calculated. As for the expected value, the derivation is based on a Gamma renewal process, meaning that $k_{ex} = k_{em} \equiv \lambda$. In the end result, λ can again be substituted for $\lambda = \frac{1}{2}k = \frac{1}{2}(k_{ex} + k_{em})$ to obtain an expression for the case where $k_{ex} \neq k_{em}$.

The following list re-states the variables that are used in the problem.

- The fluorophores emit photons with $k = k_{ex} + k_{em} = \lambda + \lambda = 2\lambda$.
- Y_j denotes the number of Poisson events in bin j. $Y_1, ..., Y_m \sim Pois(\lambda\Delta t)$.
- $U_j = Y_j \mod 2$ indicates the parity of Y_j. $U_j \sim Ber(\bar{p})$, where $\bar{p} = \frac{1-e^{-2\lambda\Delta t}}{2}$ is the probability that Y is odd.
- B_j indicates if the last Poisson event in bin j is a photon. If so, $B_j = 1$ and otherwise, $B_j = 0$. The sequence is initialized with $B_0 \sim Ber(\frac{1}{2})$ and continues as $B_j = 1 - B_{j-1}$ if $U_j = 1$, otherwise $B_j = B_{j-1}$.
- The number of photons in bin j emitted by emitter i is indicated by $X_{ij} = \frac{1}{2}Y_j + U_j(B_{j-1} - \frac{1}{2})$.
- The total photon count in bin j equals $C_j = \sum_{i=1}^{n} X_{ij}$.
- There are m bins.
- There are n emitters.
- The expected number of photons of one measurement is $N = \frac{1}{2}\lambda\Delta tnm$.
- All emitters are independent of each other, so X_{ij} and X_{kj} are independent.
- For one emitter, the photon counts per bin are dependent, so X_{ij} and X_{ik} are dependent.

The variance of eq. (3.2) for $\ell = 0$ equals

$$\begin{aligned} \mathrm{Var}(g^{(2)}[0]) &= \mathrm{Var}\left(\frac{m}{N^2}\left(\sum_{j=1}^{m} C_j^2 - N\right)\right) \\ &= \mathrm{Var}\left(\frac{m}{N^2}\sum_{j=1}^{m} C_j^2 - \frac{m}{N}\right). \end{aligned} \tag{B.1}$$

The second term, $\frac{m}{N}$, is a constant and thus, it does not influence the value of the variance. Ignoring

this factor, the expression can be rewritten as

$$\begin{aligned}\mathrm{Var}(g^{(2)}[0]) &= \mathrm{Var}\left(\frac{m}{(\frac{1}{2}\lambda\Delta t\, nm)^2}\sum_{j=1}^{m} C_j^2\right)\\ &= \left(\frac{1}{m(\frac{1}{2}\lambda\Delta t\, n)^2}\right)^2 \mathrm{Var}\left(\sum_{j=1}^{m} C_j^2\right)\\ &= \frac{1}{m^2}\left(\frac{2}{\lambda\Delta t\, n}\right)^4 \left(\mathbb{E}\left[\left(\sum_{j=1}^{m} C_j^2\right)^2\right] - \mathbb{E}\left[\sum_{j=1}^{m} C_j^2\right]^2\right).\end{aligned} \tag{B.2}$$

The second term can be derived using the expected value of C_j^2 that was calculated in eq. (3.12):

$$\begin{aligned}\frac{1}{m^2}\left(\frac{2}{\lambda\Delta t\, n}\right)^4 \mathbb{E}\left[\sum_{j=1}^{m} C_j^2\right]^2 &= \left(\frac{2}{\lambda\Delta t\, n}\right)^4 \mathbb{E}\left[C_j^2\right]^2\\ &= \left[\left(\frac{2}{\lambda\Delta t n}\right)^2 \mathbb{E}\left[C_j^2\right]\right]^2\\ &= \left[\frac{4}{\lambda^2\Delta t^2 n^2}\left(\frac{n^2\lambda^2\Delta t^2}{4} + \frac{n\lambda\Delta t}{4} + \frac{n}{4}\frac{1-e^{-2\lambda\Delta t}}{2}\right)\right]^2\\ &= \left[1 - \frac{1}{n\lambda\Delta t} + \frac{1-e^{-2\lambda\Delta t}}{2n\lambda^2\Delta t^2}\right]^2.\end{aligned} \tag{B.3}$$

However, the first term is more complex. This expression can be rewritten in terms of X_{ij} as follows

$$\begin{aligned}\mathbb{E}\left[\left(\sum_{j=1}^{m} C_j^2\right)^2\right] &= \mathbb{E}\left[\sum_{j=1}^{m} C_j^2 \sum_{l=1}^{m} C_l^2\right]\\ &= \sum_{j=1}^{m}\sum_{l=1}^{m} \mathbb{E}\left[C_j^2 C_l^2\right]\\ &= \sum_{j=1}^{m}\sum_{l=1}^{m} \mathbb{E}\left[\left(\sum_{a=1}^{n} X_{aj}\right)^2 \left(\sum_{c=1}^{n} X_{cl}\right)^2\right]\\ &= \sum_{j=1}^{m}\sum_{l=1}^{m} \mathbb{E}\left[\sum_{a=1}^{n} X_{aj} \sum_{b=1}^{n} X_{bj} \sum_{c=1}^{n} X_{cl} \sum_{d=1}^{n} X_{dl}\right]\\ &= \sum_{j=1}^{m}\sum_{l=1}^{m}\sum_{a=1}^{n}\sum_{b=1}^{n}\sum_{c=1}^{n}\sum_{d=1}^{n} \mathbb{E}\left[X_{aj}X_{bj}X_{cl}X_{dl}\right].\end{aligned} \tag{B.4}$$

This results in a sixfold summation, where j and l sum over m bins and a, b, c, and d sum over n fluorophores.

First, only the four sums over the n independent emitters are considered. Seven unique combinations of a, b, c, and d can be distinguished:

1. *abcd*

   All indices are different. There are $n!/(n-4)!$ permutations.

   All X are independent, so $\mathbb{E}\left[X_{aj}X_{bj}X_{cl}X_{dl}\right] = \mathbb{E}\left[X_{ij}\right]^4$.

2. *aacd*, *abcc*

   Two indices are the same and they are in the same bin. There are $2\cdot n!/(n-3)!$ permutations.

   $\mathbb{E}\left[X_{aj}X_{aj}X_{cl}X_{dl}\right] = \mathbb{E}\left[X_{ij}^2\right]\mathbb{E}\left[X_{ij}\right]^2$.

3. *abad*, *abca*, *abbd*, *abcb*

   Two indices are the same but they are in different bins. There are $4\cdot n!/(n-3)!$ permutations.

   $\mathbb{E}\left[X_{aj}X_{bj}X_{al}X_{dl}\right] = \mathbb{E}\left[X_{ij}X_{il}\right]\mathbb{E}\left[X_{ij}\right]^2$.

4. *aacc*

   Two times two indices are the same and they are in the same bin. There are $n!/(n-2)!$ permutations.

   $\mathbb{E}\left[X_{aj}X_{aj}X_{cl}X_{cl}\right] = \mathbb{E}\left[X_{ij}^2\right]\mathbb{E}\left[X_{ij}^2\right] = \mathbb{E}\left[X_{ij}^2\right]^2$.

5. *acac*, *acca*

   Two times two indices are the same but they are in different bins. There are $2 \cdot n!/(n-2)!$ permutations.

   $\mathbb{E}\left[X_{aj}X_{cj}X_{al}X_{cl}\right] = \mathbb{E}\left[X_{ij}X_{il}\right]^2$.

6. *aaad*, *aaca*, *abaa*, *baaa*

   Three indices are the same. There are $4 \cdot n!/(n-2)!$ permutations.

   $\mathbb{E}\left[X_{aj}X_{aj}X_{al}X_{dl}\right] = \mathbb{E}\left[X_{ij}^2X_{il}\right]\mathbb{E}\left[X_{ij}\right]$.

7. *aaaa*

   Four indices are the same. There are n permutations.

   $\mathbb{E}\left[X_{aj}X_{aj}X_{al}X_{al}\right] = \mathbb{E}\left[X_{ij}^2X_{il}^2\right]$.

The sum of all permutations adds up to n^4, as should be the case. Equation (B.4) can now be written as:

$$\begin{aligned}\mathbb{E}\left[\left(\sum_{j=1}^{m} C_j^2\right)^2\right] = \sum_{j=1}^{m}\sum_{l=1}^{m}\Bigg(&\frac{n!}{(n-4)!}\mathbb{E}\left[X_{ij}\right]^4 + \frac{2n!}{(n-3)!}\mathbb{E}\left[X_{ij}^2\right]\mathbb{E}\left[X_{ij}\right]^2 \\ &+ \frac{4n!}{(n-3)!}\mathbb{E}\left[X_{ij}X_{il}\right]\mathbb{E}\left[X_{ij}\right]^2 + \frac{n!}{(n-2)!}\mathbb{E}\left[X_{ij}^2\right]^2 \\ &+ \frac{2n!}{(n-2)!}\mathbb{E}\left[X_{ij}X_{il}\right]^2 + \frac{4n!}{(n-2)!}\mathbb{E}\left[X_{ij}^2X_{il}\right]\mathbb{E}\left[X_{ij}\right] + n\mathbb{E}\left[X_{ij}^2X_{il}^2\right]\Bigg).\end{aligned} \tag{B.5}$$

The different moments of X_{ij} are derived in appendix B.2 using the moments of Y, U and B that are calculated in appendix B.3. The moments of (combinations of) X_ij are functions of the number of emitters n, the rate λ, and the bin size Δt. In addition, some terms depend on $|j-l|$ through $e^{-2\lambda\Delta t|j-l|}$. This term represents the dependency between bin j and l of the photon count of one emitter. When bin j is close to l, the dependency is high, whereas the dependency weakens exponentially as the bins are further apart.

Equation (B.5) can be written more compactly by defining the expression in brackets as $f(|j-l|; n, \lambda, \Delta t)$, giving

$$\mathbb{E}\left[\left(\sum_{j=1}^{m} C_j^2\right)^2\right] = \sum_{j=1}^{m}\sum_{l=1}^{m} f(|j-l|; n, \lambda, \Delta t) = \sum_{j=1}^{m}\sum_{l=1}^{m} f(|j-l|). \tag{B.6}$$

The number of bins m is generally in the order of $10^4 - 10^6$, and therefore, summing all elements separately is computationally expensive. As f only depends on the absolute difference between j and l, f is the same for all combinations of j and l for which $|j-l|$ is constant. Also note that, since f only depends on $|j-l|$ through $e^{-2\lambda\Delta t|j-l|}$, f converges to a constant value quickly. The sum over j and l can thus be approximated by summing the diagonal, the first $\nu \approx 100$ off-diagonals and by summing the remainder (fig. 15), giving

$$\mathbb{E}\left[\left(\sum_{j=1}^{m} C_j^2\right)^2\right] = m \cdot f(0) + 2\sum_{\xi=1}^{\nu}(m-\xi)\cdot f(\xi) + \left((m-\nu)^2 - (m-\nu)\right) f(\infty). \tag{B.7}$$

The variance of the coherence can now be found by substituting expressions eq. (B.3) and eq. (B.7) into equation eq. (B.2).

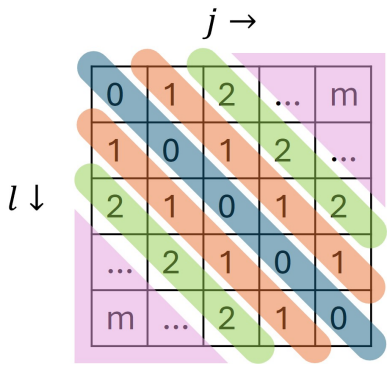

Figure 15: The matrix shows $|j-l|$. The value of $f(|j-l|)$ is constant for each (off-)diagonal. When $|j-l|$ is large, $f(|j-l|)$ converges to a constant, and thus every matrix element in the pink triangle has approximately the same value.

B.2 Moments of X

In this section, the moments of X_{ij} and products of multiple X_{ij} that are needed for eq. (B.5) are derived. A distinction is made between products of X for equal and different values of j and l. The result is written in terms of Y and U. Moments of B are substituted for their value in the derivations. All moments of Y, U, and B and their products can be found in appendix B.3.

- $\mathbb{E}[X_{ij}] = \mathbb{E}[\frac{1}{2}Y_j + U_j(B_{j-1} - \frac{1}{2})] = \frac{1}{2}\mathbb{E}[Y_j] + 0 = \frac{1}{2}\mathbb{E}[Y]$

In the case that $l = j$:

- $\mathbb{E}\left[X_{ij}X_{il}\right] = \mathbb{E}[X_{ij}^2] = \frac{1}{4}(\mathbb{E}[Y^2] + \mathbb{E}[U])$.

$$\begin{aligned}\mathbb{E}[X_{ij}^2] &= \mathbb{E}[\tfrac{1}{4}Y_j^2 + Y_jU_j(B_{j-1} - \tfrac{1}{2}) + U_j^2(B_{j-1} - \tfrac{1}{2})^2] \\ &= \tfrac{1}{4}\mathbb{E}[Y_j^2] + \tfrac{1}{4}\mathbb{E}[U_j^2]\end{aligned}$$

- $\mathbb{E}\left[X_{ij}^2X_{il}\right] = \mathbb{E}[X_{ij}^3] = \frac{1}{8}\mathbb{E}[Y^3] + \frac{3}{8}\mathbb{E}[YU]$.

$$\begin{aligned}\mathbb{E}[X_{ij}^3] &= \mathbb{E}[\tfrac{1}{8}Y_j^3 + \tfrac{3}{4}Y_j^2U_j(B_{j-1} - \tfrac{1}{2}) + \tfrac{3}{2}Y_jU_j^2(B_{j-1} - \tfrac{1}{2})^2 + U_j^3(B_{j-1} - \tfrac{1}{2})^3] \\ &= \tfrac{1}{8}\mathbb{E}[Y_j^3] + 0 + \tfrac{3}{2}\mathbb{E}[Y_jU_j^2] \cdot \tfrac{1}{4} + 0 \\ &= \tfrac{1}{8}\mathbb{E}[Y_j^3] + \tfrac{3}{8}\mathbb{E}[Y_jU_j^2]\end{aligned}$$

- $\mathbb{E}\left[X_{ij}^2X_{il}^2\right] = \mathbb{E}[X_{ij}^4] = \frac{1}{16}\mathbb{E}[Y^4] + \frac{3}{8}\mathbb{E}[Y^2U^2] + \frac{1}{16}\mathbb{E}[U]$.

$$\begin{aligned}\mathbb{E}[X_{ij}^4] &= \mathbb{E}[\tfrac{1}{16}Y_j^4 + 4\tfrac{1}{8}Y_j^3U_j(B_{j-1} - \tfrac{1}{2}) + 6\tfrac{1}{4}Y_j^2U_j^2(B_{j-1} - \tfrac{1}{2})^2 + 4\tfrac{1}{2}Y_jU_j^3(B_{j-1} - \tfrac{1}{2})^3 + U_j^4(B_{j-1} - \tfrac{1}{2})^4] \\ &= \tfrac{1}{16}\mathbb{E}[Y_j^4] + 0 + \tfrac{6}{4}\mathbb{E}[Y_j^2U_j^2] \cdot \tfrac{1}{4} + 0 + \mathbb{E}[U_j^4] \cdot \tfrac{1}{16} \\ &= \tfrac{1}{16}\mathbb{E}[Y_j^4] + \tfrac{6}{16}\mathbb{E}[Y_j^2U_j^2] + \tfrac{1}{16}\mathbb{E}[U_j^4]\end{aligned}$$

In the case that $l \neq j$:

- $\mathbb{E}\left[X_{ij}X_{il}\right] = \frac{1}{4}\mathbb{E}[Y]^2 + \frac{1}{4}\mathbb{E}[U]^2 \cdot e^{-2\lambda\Delta t|j-l|}$.

$$\begin{aligned}\mathbb{E}\left[X_{ij}X_{il}\right] &= \mathbb{E}[\tfrac{1}{4}Y_jY_l + \tfrac{1}{2}Y_jU_l(B_{l-1} - \tfrac{1}{2}) + \tfrac{1}{2}Y_lU_j(B_{j-1} - \tfrac{1}{2}) + U_j(B_{j-1} - \tfrac{1}{2})U_l(B_{l-1} - \tfrac{1}{2})] \\ &= \tfrac{1}{4}\mathbb{E}[Y_j]^2 + 0 + 0 + \mathbb{E}[U_j]^2\mathbb{E}[(B_{j-1} - \tfrac{1}{2})(B_{l-1} - \tfrac{1}{2})] \\ &= \tfrac{1}{4}\mathbb{E}[Y_j]^2 + \mathbb{E}[U_j]^2 \cdot \tfrac{1}{4}e^{-2\lambda\Delta t|j-l|}\end{aligned}$$

- $\mathbb{E}\left[X_{ij}^2 X_{il}\right] = \frac{1}{8}\mathbb{E}[Y](\mathbb{E}[Y^2] + \mathbb{E}[U]) + \frac{1}{4}\mathbb{E}[YU]\mathbb{E}[U] \cdot e^{-2\lambda\Delta t|j-l|}$.

$$\begin{aligned}
\mathbb{E}\left[X_{ij}^2 X_{il}\right] &= \mathbb{E}[\tfrac{1}{4}Y_j^2 \cdot \tfrac{1}{2}Y_l + \tfrac{1}{4}Y_j^2 \cdot U_l(B_{l-1} - \tfrac{1}{2}) + Y_j U_j(B_{j-1} - \tfrac{1}{2}) \cdot \tfrac{1}{2}Y_l \\
&\quad + Y_j U_j(B_{j-1} - \tfrac{1}{2}) \cdot U_l(B_{l-1} - \tfrac{1}{2}) + U_j^2(B_{j-1} - \tfrac{1}{2})^2 \cdot \tfrac{1}{2}Y_l \\
&\quad + U_j^2(B_{j-1} - \tfrac{1}{2})^2 \cdot U_l(B_{l-1} - \tfrac{1}{2})] \\
&= \tfrac{1}{8}\mathbb{E}[Y_j^2]\mathbb{E}[Y_l] + 0 + 0 \\
&\quad + \mathbb{E}[Y_j U_j]\mathbb{E}[U_l]\mathbb{E}[(B_{j-1} - \tfrac{1}{2})(B_{l-1} - \tfrac{1}{2})] + \tfrac{1}{2}\mathbb{E}[U_j^2]\mathbb{E}[Y_l]\mathbb{E}[(B_{j-1} - \tfrac{1}{2})^2] \\
&\quad + \mathbb{E}[U_j^2]\mathbb{E}[U_l]\mathbb{E}[(B_{j-1} - \tfrac{1}{2})^2(B_{l-1} - \tfrac{1}{2})] \\
&= \tfrac{1}{8}\mathbb{E}[Y_j^2]\mathbb{E}[Y_l] + \mathbb{E}[Y_j U_j]\mathbb{E}[U_l] \cdot \tfrac{1}{4}e^{-2\lambda\Delta t|j-l|} + \tfrac{1}{2}\mathbb{E}[U_j^2]\mathbb{E}[Y_l] \cdot \tfrac{1}{4} + 0
\end{aligned}$$

- $\mathbb{E}\left[X_{ij}^2 X_{il}^2\right] = \frac{1}{16}(\mathbb{E}[Y^2]^2 + \mathbb{E}[U]^2) + \frac{1}{8}\mathbb{E}[Y^2]\mathbb{E}[U] + \frac{1}{16}\mathbb{E}[YU]^2 \cdot e^{-2\lambda\Delta t|j-l|}$.

$$\begin{aligned}
\mathbb{E}[X_{ij}^2 X_{il}^2] &= \mathbb{E}[\tfrac{1}{16}Y_j^2 Y_l^2 + \tfrac{1}{4}Y_j^2 \cdot \tfrac{1}{2}Y_l U_l(B_{l-1} - \tfrac{1}{2}) + \tfrac{1}{4}Y_j^2 U_l^2(B_{l-1} - \tfrac{1}{2})^2 \\
&\quad + \tfrac{1}{2}Y_j U_j(B_{j-1} - \tfrac{1}{2}) \cdot \tfrac{1}{4}Y_l^2 + \tfrac{1}{2}Y_j U_j(B_{j-1} - \tfrac{1}{2}) \cdot \tfrac{1}{2}Y_l U_l(B_{l-1} - \tfrac{1}{2}) \\
&\quad + \tfrac{1}{2}Y_j U_j(B_{j-1} - \tfrac{1}{2})U_l^2(B_{l-1} - \tfrac{1}{2})^2 \\
&\quad + U_j^2(B_{j-1} - \tfrac{1}{2})^2 \cdot \tfrac{1}{4}Y_l^2 + U_j^2(B_{j-1} - \tfrac{1}{2})^2 \cdot \tfrac{1}{2}Y_l U_l(B_{l-1} - \tfrac{1}{2}) \\
&\quad + U_j^2(B_{j-1} - \tfrac{1}{2})^2 \cdot U_l^2(B_{l-1} - \tfrac{1}{2})^2 \\
&= \tfrac{1}{16}\mathbb{E}[Y_j^2]^2 + 0 + \tfrac{1}{4}\mathbb{E}[Y_j^2]\mathbb{E}[U_l^2] \cdot \tfrac{1}{4} + 0 + \tfrac{1}{4}\mathbb{E}[Y_j U_j]^2 \cdot \tfrac{1}{4}e^{-2\lambda\Delta t|j-l|} + 0 \\
&\quad + \tfrac{1}{4}\mathbb{E}[Y_l^2]\mathbb{E}[U_j^2] \cdot \tfrac{1}{4} + 0 + \mathbb{E}[U_j^2]^2 \cdot \tfrac{1}{16} \\
&= \tfrac{1}{16}\mathbb{E}[Y_j^2]^2 + \tfrac{1}{8}\mathbb{E}[Y_j^2]\mathbb{E}[U_j^2] + \tfrac{1}{16}\mathbb{E}[Y_j U_j]^2 \cdot e^{-2\lambda\Delta t|j-l|} + \tfrac{1}{16}\mathbb{E}[U_j^2]^2
\end{aligned}$$

B.3 Auxiliary Moments

B.3.1 Moments of Y

Y is a Poisson distributed variable with rate $\lambda\Delta t$. The first four raw moments thus equal:

- $\mathbb{E}[Y] = \lambda\Delta t$
- $\mathbb{E}[Y^2] = (\lambda\Delta t)^2 + \lambda\Delta t$
- $\mathbb{E}[Y^3] = (\lambda\Delta t)^3 + 3(\lambda\Delta t)^2 + \lambda\Delta t$
- $\mathbb{E}[Y^4] = (\lambda\Delta t)^4 + 6(\lambda\Delta t)^3 + 7(\lambda\Delta t)^2 + \lambda\Delta t$.

B.3.2 Moments of U

U is a Bernoulli random variable with a probability of success equal to $\bar{p} = (1 - e^{-2\lambda\Delta t)})/2$. Therefore, all raw moments are equal to $\bar{p}$:

$$\mathbb{E}[U^k] = \mathbb{E}[U] = \bar{p}.$$

B.3.3 Moments of Combinations of Y and U

- $\mathbb{E}[YU] = \bar{p} \cdot \lambda\Delta t \left(\frac{1+e^{-2\lambda\Delta t}}{1-e^{-2\lambda\Delta t}}\right)$. Using the total law of expectation,

$$\begin{aligned}
\mathbb{E}[YU] &= \mathbb{E}[\mathbb{E}[YU|U]] \\
&= \mathbb{P}(U=0)\mathbb{E}[Y \cdot 0|U=0] + \mathbb{P}(U=1)\mathbb{E}[Y \cdot 1|U=1] \\
&= 0 + \bar{p} \cdot \mathbb{E}[Y|U=1] \\
&= \bar{p} \cdot \mathbb{E}[Y|Y \text{ is odd}] \\
&= \bar{p} \cdot \sum_y y\mathbb{P}(Y=y|Y \text{ odd}).
\end{aligned} \tag{B.8}$$

In the penultimate step, it was used that U_i is defined as $Y_i \mod 2$. Thus, $\mathbb{E}[Y|U=1]$ is the expected value of the odd values that Y assumes ($\mathbb{E}[Y|Y \text{ is odd}]$). The conditional probability of Y is

$$\mathbb{P}(Y=y|Y \text{ odd}) = \frac{\mathbb{P}(Y=y \cap Y \text{ odd})}{\mathbb{P}(Y \text{ odd})} = \begin{cases} 0 & y \text{ even} \\ \frac{\mathbb{P}(Y=y)}{\mathbb{P}(Y \text{ odd})} = \frac{(y!)^{-1}(\lambda\Delta t)^y e^{-\lambda\Delta t}}{\frac{1}{2}(1-e^{-2\lambda\Delta t})} = \frac{2(\lambda\Delta t)^y}{y!(e^{\lambda\Delta t}-e^{-\lambda\Delta t})} & y \text{ odd}. \end{cases} \tag{B.9}$$

By substituting this expression in eq. (B.8), we find the expected value of YU:

$$\begin{aligned} \mathbb{E}[YU] &= \bar{p} \cdot \sum_{y \text{ odd}} y \frac{2(\lambda\Delta t)^y}{y!(e^{\lambda\Delta t}-e^{-\lambda\Delta t})} \\ &= \bar{p} \cdot \frac{2}{e^{\lambda\Delta t}-e^{-\lambda\Delta t}} \sum_{n \text{ odd}} \frac{y(\lambda\Delta t)^y}{y!} \\ &= \bar{p} \cdot \frac{2}{e^{\lambda\Delta t}-e^{-\lambda\Delta t}} \sum_{y \text{ odd}} \frac{(\lambda\Delta t)^y}{(y-1)!} \\ &= \bar{p} \cdot \frac{2\lambda\Delta t}{e^{\lambda\Delta t}-e^{-\lambda\Delta t}} \sum_{y \text{ even}} \frac{(\lambda\Delta t)^y}{y!} \\ &= \bar{p} \cdot \lambda\Delta t \left(\frac{1+e^{-2\lambda\Delta t}}{1-e^{-2\lambda\Delta t}}\right). \end{aligned} \tag{B.10}$$

- $\mathbb{E}[YU^k] = \mathbb{E}[YU] = \bar{p} \cdot \lambda\Delta t \left(\frac{1+e^{-2\lambda\Delta t}}{1-e^{-2\lambda\Delta t}}\right)$, following the same logic as for $\mathbb{E}[YU]$.
- $\mathbb{E}[Y^2U^2] = \bar{p} \cdot \left((\lambda\Delta t)^2 + \lambda\Delta t \left(\frac{1+e^{-2\lambda\Delta t}}{1-e^{-2\lambda\Delta t}}\right)\right)$. Using the total law of expectation,

$$\begin{aligned} \mathbb{E}[Y^2U^2] &= \mathbb{P}(U=0)\mathbb{E}[Y^2 \cdot 0|U=0] + \mathbb{P}(U=1)\mathbb{E}[Y^2 \cdot 1|U=1] \\ &= 0 + \bar{p} \cdot \mathbb{E}[Y^2|U=1] \\ &= \bar{p} \cdot \mathbb{E}[Y^2|Y \text{ odd}] \\ &= \bar{p} \cdot \sum_y y^2 \mathbb{P}(Y=y|Y \text{ odd}) \\ &= \bar{p} \cdot \sum_{y \text{ odd}} y^2 \frac{2(\lambda\Delta t)^y}{y!(e^{\lambda\Delta t}-e^{-\lambda\Delta t})} \\ &= \bar{p} \cdot \frac{2}{e^{\lambda\Delta t}-e^{-\lambda\Delta t}} \sum_{y \text{ odd}} y^2 \frac{(\lambda\Delta t)^y}{y!} \\ &= \bar{p} \cdot \frac{2\lambda\Delta t}{e^{\lambda\Delta t}-e^{-\lambda\Delta t}} \left(\cosh(\lambda\Delta t) + \lambda\Delta t \sinh(\lambda\Delta t)\right) \\ &= \bar{p} \cdot \left((\lambda\Delta t)^2 + \lambda\Delta t \left(\frac{1+e^{-2\lambda\Delta t}}{1-e^{-2\lambda\Delta t}}\right)\right) \end{aligned} \tag{B.11}$$

B.3.4 Moments of B

B is a Bernoulli random variable with an expected value of $\frac{1}{2}$.

- $\mathbb{E}[B^k] = \mathbb{E}[B] = \frac{1}{2}$
- $\mathbb{E}[B - \frac{1}{2}] = 0$
- $\mathbb{E}[(B_i - \frac{1}{2})^2] = \mathbb{E}[B_i^2 - B_i + \frac{1}{4}] = \frac{1}{4}$
- $\mathbb{E}[(B_i - \frac{1}{2})^3] = \mathbb{E}[B_i^3 - 3\frac{1}{2}B_i^2 + 3\frac{1}{4}B_i - \frac{1}{8}] = \frac{1}{2} - \frac{3}{4} + \frac{3}{8} - \frac{1}{8} = 0$
- $\mathbb{E}[(B_i - \frac{1}{2})^4] = \mathbb{E}[B_i^4 - 4\frac{1}{2}B_i^3 + 6\frac{1}{4}B_i^2 - 4\frac{1}{8}B_i + \frac{1}{16}] = \frac{1}{2} - \frac{4}{4} + \frac{6}{8} - \frac{4}{16} + \frac{1}{16} = \frac{1}{16}$

B.3.5 Moments of Multiple B

B_i is dependent on $B_{k<i}$. This dependence can be described through a discrete-time Markov chain on $\{0, 1\}$. The transition matrix is given by

$$P = \begin{pmatrix} p & \bar{p} \\ \bar{p} & p \end{pmatrix} \tag{B.12}$$

where $p = \mathbb{P}(Y \text{ even}) = \frac{1}{2}(1 + e^{-2\lambda\Delta t})$ and $\bar{p} = \mathbb{P}(Y \text{ odd}) = \frac{1}{2}(1 - e^{-2\lambda\Delta t})$. The stationary distribution is $(0.5, 0.5)$. The n-step transition probabilities are

$$p_{00}^{(n)} = p_{11}^{(n)} = \tfrac{1}{2} + \tfrac{1}{2}(2p-1)^n = \tfrac{1}{2} + e^{-2\lambda\Delta tn} \tag{B.13}$$

and

$$p_{01}^{(n)} = p_{10}^{(n)} = \tfrac{1}{2} - \tfrac{1}{2}(2p-1)^n = \tfrac{1}{2} - e^{-2\lambda\Delta tn}. \tag{B.14}$$

- $\mathbb{E}[B_iB_j] = 0 + 0 + 0 + \mathbb{P}(B_i = B_j = 1) \cdot 1 \cdot 1 = \frac{1}{2}p_{11}^{(|i-j|)} = \frac{1}{4} + \frac{1}{4}e^{-2\lambda\Delta t|i-j|}$
- $\mathbb{E}[(B_i - \frac{1}{2})(B_j - \frac{1}{2})] = \mathbb{E}[B_iB_j - \frac{1}{2}B_i - \frac{1}{2}B_j + \frac{1}{4})] = \mathbb{E}[B_iB_j] - \frac{1}{4} - \frac{1}{4} + \frac{1}{4} = \frac{1}{4}e^{-2\lambda\Delta t|i-j|}$
- $\mathbb{E}[(B_i - \frac{1}{2})^2(B_j - \frac{1}{2})] = 0$

$$\begin{aligned}
\mathbb{E}[(B_i - \tfrac{1}{2})^2(B_j - \tfrac{1}{2})] &= \mathbb{E}[B_i^2B_j - \tfrac{1}{2}B_i^2 - B_iB_j + \tfrac{1}{2}B_i + \tfrac{1}{4}B_j - \tfrac{1}{8}] \\
&= \mathbb{E}[B_i^2B_j] - \tfrac{1}{4} - \mathbb{E}[B_iB_j] + \tfrac{1}{4} + \tfrac{1}{8} - \tfrac{1}{8} \\
&= \mathbb{P}(B_i = B_j = 1) - \mathbb{P}(B_i = B_j = 1) \\
&= 0
\end{aligned}$$

- $\mathbb{E}[(B_i - \frac{1}{2})^2(B_j - \frac{1}{2})^2] = \frac{1}{16}$. In the following derivation, all products of B_iB_j cancel out.

$$\begin{aligned}
\mathbb{E}[(B_i - \tfrac{1}{2})^2(B_j - \tfrac{1}{2})^2] &= \mathbb{E}[B_i^2B_j^2 - B_i^2B_j + \tfrac{1}{4}B_i^2 - B_iB_j + B_iB_j - \tfrac{1}{4}B_i + \tfrac{1}{4}B_j^2 - \tfrac{1}{4}B_j + \tfrac{1}{16}] \\
&= \tfrac{1}{8} - \tfrac{1}{8} + \tfrac{1}{8} - \tfrac{1}{8} - \tfrac{1}{16} \\
&= \tfrac{1}{16}
\end{aligned}$$